Agricultural and Forest Meteorology 388 (2026) 111357

Contents lists available at ScienceDirect

Agricultural and Forest Meteorology

journal homepage: www.elsevier.com/locate/agrformet

Estimating whole-tree sap flow in buttressed and irregular trunks

Michael W. Burnett [a,*], Rayna Ruggeri [a], Kelly K. Caylor [b,c], Hillary S. Young [a], Leander D.L. Anderegg [a]

[a] Department of Ecology, Evolution, and Marine Biology, University of California Santa Barbara, Santa Barbara, CA, 93106, USA
[b] Department of Geography, University of California Santa Barbara, Santa Barbara, CA, 93106, USA
[c] Bren School of Environmental Science and Management, University of California Santa Barbara, Santa Barbara, CA, 93106, USA

ARTICLE INFO

Keywords:
Ecohydrology
Transpiration
Tropical atoll
Heat pulse velocity
Heat ratio method
Heartwood

ABSTRACT

Sap flow sensors measure the movement of sap (J_s, sap flux density) at discrete points within a tree trunk. Upscaling these measurements to estimate the water consumption of an entire tree (*SF*, whole-tree sap flow) typically requires assuming the trunk's cross section is perfectly circular. This assumption will overestimate the area and underestimate the perimeter of a real trunk's cross section. But how might it bias sap flow estimates in trees with irregularly shaped trunks?

We digitized trunk cross sections from *Pisonia grandis*, a tropical canopy tree that exhibits diverse trunk shapes, and compared sap flow from the traditional circular model (SF_{circ}) to a spatially explicit reference model (SF_{ref}) for a wide array of radial sap flux density profiles. Depending on the profile, we found that the circular assumption may underestimate sap flow by more than 25% or overestimate it by over 50% in the most irregular *Pisonia* trunks.

To mitigate these biases, we recommend measuring a trunk's perimeter in addition to its diameter at breast height (DBH). These measurements enable the calculation of the trunk's perimeter convexity (c_p), which strongly predicted sap flow bias in *Pisonia* ($r^2 = 0.961$) from the circular trunk assumption. Simulations show that for radial sap flux profiles typical of dicots, bias should remain within ±5% when $c_p \geq 0.96$. For trees with $c_p < 0.96$, we introduce two new upscaling models that can significantly decrease sap flow biases. The most sophisticated model reduced bias to within ±5% for 31 of 33 tested trees with c_p values as low as 0.68 and requires just one additional field measurement, the depth of the deepest trunk concavity. These corrected sap flow models are available in a new R package, sapscaleR.

1. Introduction

Measurements of sap flux density (J_s, sometimes called sap velocity[1]) are commonly used to estimate the water consumption rates of woody plants. Sap flow sensors produce these measurements at discrete points within the trunk, meaning they must be integrated across the cross-sectional area of the trunk (A_0) to reflect the total volumetric flow of water through the plant (*SF*, whole-plant sap flow)(Edwards et al., 1996).

Trunk area is typically approximated with a taut tape stretched around the trunk 1.3 m above the ground. Scaling the tape length by $1/\pi$ provides the diameter at breast height (DBH); dividing DBH by two yields a radius from which a circular area can be calculated.

DBH-derived estimates of trunk area thus assume a trunk's cross section is a perfect circle. We term this assumption the *circular trunk assumption*. But DBH measurements actually record the trunk's convex hull perimeter (P_h), and trunk areas calculated from these measurements represent a circle with a circumference equal to P_h.

The ease of measuring DBH has made it a standard metric of tree size. But the implicitly assumed circle will always underestimate the perimeter (P_0) of a non-convex trunk cross section and overestimate the area of any cross section that is not perfectly circular.

For many species, the circular trunk assumption is reasonable and the resulting errors negligible. However, tropical forest trees feature root buttresses and irregular trunk morphologies much more frequently than those growing at higher latitudes (Hallé et al., 1978; Smith, 1972).

* Corresponding author.
E-mail address: mburnett@ucsb.edu (M.W. Burnett).

[1] We follow Steppe et al. (2010) assertion that the use of heat pulse velocities to quantify sap transport results in units of volumetric flux density [$L^3\,L^{-2}\,T^{-1}$] rather than units of velocity [$L\,T^{-1}$]. The choice of units does not affect the mathematics presented in this paper.

https://doi.org/10.1016/j.agrformet.2026.111357
Received 6 February 2026; Received in revised form 6 July 2026; Accepted 8 July 2026
Available online 22 July 2026
0168-1923/

In some tropical forests, as many as 32% of individuals and 68% of species feature root buttresses (He et al., 2013). The application of the circular trunk assumption to such complex tree morphologies warrants closer examination.

We first ask: *how problematic might it be to assume that tree trunks are perfectly round?* In extreme cases, the circular trunk assumption can overestimate trunk area by over 400% (Nogueira et al., 2006) and underestimate trunk perimeter by 35% (Dean et al., 2003). Even so, estimates of sap flow created by upscaling sap flux density measurements universally rely upon the circular trunk assumption, and to our knowledge no study has examined the downstream effects of these geometric errors on sap flow estimates. Clearly significant biases are possible, but their magnitude and direction will depend on the trunk's shape and distribution of sap flux.

We next ask: for irregular trunks whose assumed-circle sap flow (SF_{circ}) is intolerably biased, *how can sap flow be accurately estimated from sap flux density measurements?* The traditional formula for integrating a flux over a circular area (Edwards and Warwick, 1984; Green and Clothier, 1988) no longer applies. Sap flow sensors might be installed above root buttresses to access a more circular trunk section, but many tropical trees (including the species studied here) feature irregular trunk shapes well above the ground. Installing sensors at elevated positions also may not always be possible or practical.

In this study we approach both questions using 33 digitized trunk cross sections from *Pisonia grandis* R.Br. (Nyctaginaceae), a dominant canopy tree in tropical atoll forests (Burnett et al., 2024; Wiens, 1962). *Pisonia* exhibits a wide range of trunk morphologies due to its buttressed roots, low branching habit, and tendency for inosculation and limb fusing (Cribb, 1969). *Pisonia* trees grow quickly and fall frequently because of their soft wood, but fallen logs rapidly produce new shoots that can fuse to create highly irregular trunk shapes (Burger, 2005). The largest individuals can attain heights of 25 m and DBHs of 3.5 m (Batianoff, 1999; Rock, 1916; Walker, 1991).

To estimate the sap flow bias that results from the circular trunk assumption, we compare SF_{circ} to reference sap flow (SF_{ref}) estimates modeled spatially within each digitized cross section. By simulating a wide array of radial sap flux density profiles, we derive the full range of sap flow biases possible for each trunk, illuminating the relationships between trunk shape, sap flux distribution, and sap flow bias.

We next attempt to correct SF_{circ} for irregular trunk cross sections, deriving theoretical ($SF_{steiner}$) and semi-empirical (SF_{corr}) formulae for estimating sap flow with minimal additional field measurements. We then test these models using sap flux density data from heat pulse velocity sap flow sensors deployed on Teti'aroa Atoll, French Polynesia.

Finally, we propose a workflow for future sap flow studies of irregular tree trunks (Fig. 1). It requires only 1–2 additional field measurements (trunk perimeter and deepest concavity depth), can be applied to any radial sap flux density profile, and is based primarily on the trunk's perimeter convexity (c_p), an intuitive metric of complexity (Zunic and Rosin, 2004).

2. Theory

In this section we review the traditional circular method for upscaling sap flux density measurements to whole-tree sap flow, investigate the mechanisms by which this method may become biased in irregular trunks, and explore alternative upscaling approaches that do not rely upon the circular trunk assumption.

2.1. Within-trunk spatial variability of sap flux density (J_s)

The problem at hand is to upscale sap flux density J_s, the volumetric flux density per cross-sectional area of sapwood [L^3 L^{-2} T^{-1}], to whole-tree sap flow SF, a volumetric flowrate [L^3 T^{-1}], by multiplying by the cross-sectional area A_0 [L^2] (Marshall, 1958).

For the present study we ignore temporal variations in sap flux density (Caylor and Dragoni, 2009) to instead focus on its spatial variability within a tree's trunk.

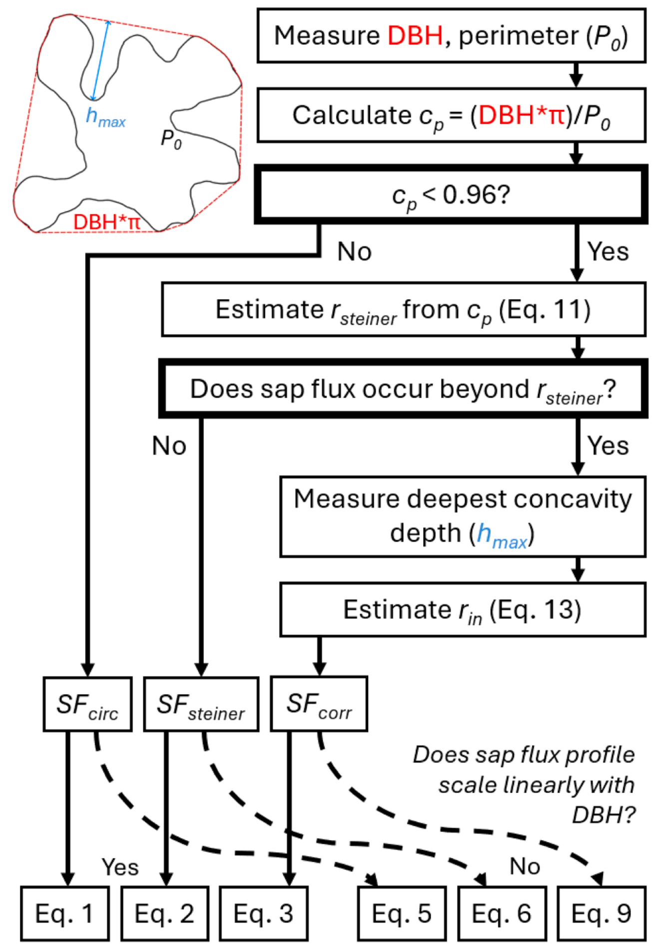

Fig. 1. Flowchart illustrating the proposed workflow for estimating sap flow in irregular trunks.

This spatial variability can be separated into radial (from the cambium to the trunk center) and azimuthal/circumferential (in different directions around the trunk center) components. Radial sap flux density profiles ("sap flux profiles" for brevity) are commonly measured using probes with temperature sensors installed at multiple depths in the trunk, but azimuthal variability is less frequently quantified and usually ignored despite being comparable in magnitude to radial variability (López-Bernal et al., 2010; Lu et al., 2000; Merlin et al., 2020; Shinohara et al., 2013).

A common sampling strategy involves installing one sensor per tree across more individual trees rather than instrumenting fewer individuals with multiple sensors, essentially capturing the azimuthal variability of sap flux density within the tree-to-tree variability while still quantifying radial variability (Komatsu et al., 2017). In this study we adopt the assumption of azimuthally constant sap flux densities to remain consistent with this practice and clarify the calculation of sap flow.

2.2. The circular method for estimating sap flow (SF_{circ})

Under the circular trunk assumption, a trunk's cross section is the circle whose circumference equals the convex hull perimeter, P_h. This assumption enables a simple integral method for upscaling radial sap flux profiles to $\boldsymbol{SF_{circ}}$ using DBH data (Caylor and Dragoni, 2009; Edwards and Warwick, 1984; Green and Clothier, 1988).

Consider a perfectly circular trunk cross section (the *assumed circle*) with radius R_{circ} and circumference $P_0 = 2\pi R_{circ}$. Let r denote the relative

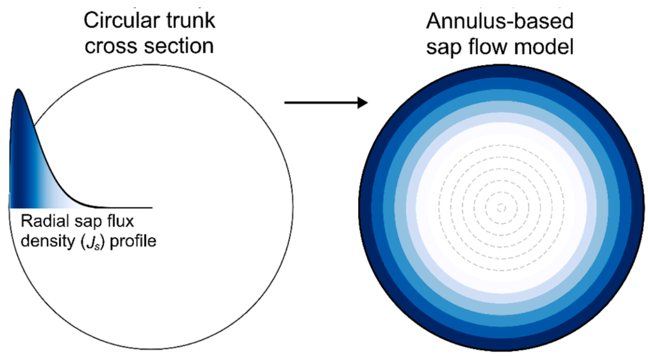

Fig. 2. A theoretical circular trunk cross section and its radial J_s profile (left). Whole-tree sap flow can be approximated by partitioning the circle into nested annuli of equal thickness and summing their areas, with each weighted by its respective J_s (right). Darker shades of blue denote greater J_s; annuli with no sap flux (heartwood) are drawn with grey dashed lines.

radial depth from the circle's edge ($r = 0$) toward its center ($r = 1$) and $J_s(r)$ the sap flux density at depth r.

To produce SF_{circ}, we must integrate the radial sap flux density function $J_s(r)$ over the trunk area. Conceptually, one can picture this process as dividing the assumed circle into many thin nested annuli, multiplying the area of each annulus by its average local J_s to estimate its annular volumetric sap flow, and summing all annular sap flows to produce whole-tree sap flow SF (Fig. 2).

Eq. (1) is the integral form of this summation as presented in Link et al. (2020). Functionally, the $(1 - r)$ term in the integrand reflects the linear decay of annulus areas with increasing r—a special property of circles. The $2\pi R_{circ}^2$ prefactor scales the dimensionless annular area term $(1 - r)$ to proper spatial units. A more detailed derivation of SF_{circ} may be found in Appendix A.

$$SF_{circ} = 2\pi R_{circ}^2 \int_0^1 J_s(r)(1 - r)dr \tag{1}$$

2.3. Correcting SF_{circ} for use in non-convex trunks

Now consider a non-convex cross section of a tree trunk. Its assumed circle is the circle whose circumference equals the trunk's convex hull perimeter, P_h. Thus, the trunk's true perimeter, P_0, is longer than that of its assumed circle (P_{circ}). Its area, A_0, is smaller than that of its assumed circle (Fig. 3).

Notice that in Fig. 3, the trunk's outermost annulus is larger by area than the circle's outermost annulus (darkest blue layers), but that the trunk's inner annuli (light blue layers) are much smaller than their circular counterparts. While the trunk's longer perimeter leads to larger shallow annuli than in the assumed circle, its concavities produce extensive areas of self-intersection when the shape is eroded, leaving deeper annuli smaller than those of the circle.

Annular areas in a non-convex polygon decay linearly with r until the depth at which significant topological changes (self-intersections) first occur. These topological changes cause deviations from Steiner's formulae (Gray, 2004), which relate the perimeters and areas of parallel offset (eroded) sets and form the basis of SF_{circ} (see Appendix A). Once induced, such topological changes accelerate the decay of annular areas with r.

But for sufficiently shallow depths (i.e. where r is smaller than the shallowest depth of major topological changes), SF_{circ} can be modified with perimeter convexity $c_p = P_h/P_0$ (Zunic and Rosin, 2004) to produce $\boldsymbol{SF_{steiner}}$ (Eq. (2)), which appropriately expands shallow annulus areas and steepens their decay as r increases:

$$SF_{steiner} = \frac{2\pi R_{circ}^2}{c_p} \int_0^1 J_s(r)(1 - c_p r)dr \tag{2}$$

But how shallow is sufficiently shallow to use $SF_{steiner}$? We designate the relative depth of the shallowest significant topological changes $\boldsymbol{r_{steiner}}$. In other words, Steiner's formulae are valid even in non-convex polygons for $r \leq r_{steiner}$, meaning $SF_{steiner}$ (Eq. (2)) will accurately estimate sap flow if $J_s(r)$ is mostly zero for $r > r_{steiner}$.

Therefore, $SF_{steiner}$ is valid for trunks in which sap transport is confined to shallow depths. This condition is true for many dicot trees, but there exist exceptions (Berdanier et al., 2016; Link et al., 2020). If a tree exhibits significant sap transport deeper than $r_{steiner}$, an expanded sap flow model that characterizes annular areas across the full range of r is needed.

To create such a model, we must account for another transition in the annuli produced by eroding the trunk. Notice that when dividing the trunk cross section and its assumed circle into nested annuli of consistent thickness, the real trunk produces far fewer annuli than does the circle (Fig. 3). This fact stems from the circular trunk assumption—r is always defined by R_{circ}, which is a theoretical depth that will never be reached by the erosion of a non-circular polygon. The depth to which annuli of equal thickness can be nested within a polygon is determined by the radius of the largest possible inscribed circle (R_{in}). In other words, once r reaches $\boldsymbol{r_{in}} = R_{in} / R_{circ}$, annular areas drop to zero.

Fig. 4a depicts annular areas (normalized to the outermost annulus area of the assumed circle) from real, non-convex tree trunks as a function of r. Three domains become apparent: the near-linear domain approximated by $SF_{steiner}$, a domain of steeper decay once $r_{steiner}$ is crossed, and a domain where annular areas equal zero once r_{in} is crossed (Fig. 4b). In the middle domain, annular areas decrease monotonically to zero. By assuming this decrease is linear, we produce a piecewise integral model we designate $\boldsymbol{SF_{corr}}$ (Eq. (3)):

$$SF_{corr} = \frac{2\pi R_{circ}^2}{c_p} \left(\int_0^{r_{steiner}} (1 - c_p r) J_s(r)\, dr + \int_{r_{steiner}}^{r_{in}} (1 - c_p r_{steiner}) \frac{r_{in} - r}{r_{in} - r_{steiner}} J_s(r)\, dr \right) \tag{3}$$

Obviously, applying Eq. (3) requires knowledge of r_{in} and $r_{steiner}$. These depths cannot be computed from simple geometric properties of a tree trunk, so we empirically model them using our 33 digitized *Pisonia grandis* trunks (see Sections 3.4.3,4.3).

More detailed derivations of Eqs. (1)-(3) are available in Appendix A.

2.4. Summary: sources of bias in SF_{circ}

In summary, sap flow estimation biases resulting from the circular trunk assumption can be attributed to three effects:

1. In non-convex trunk cross sections, the true perimeter is greater than the hull perimeter. Annular areas at shallow depths are thus greater

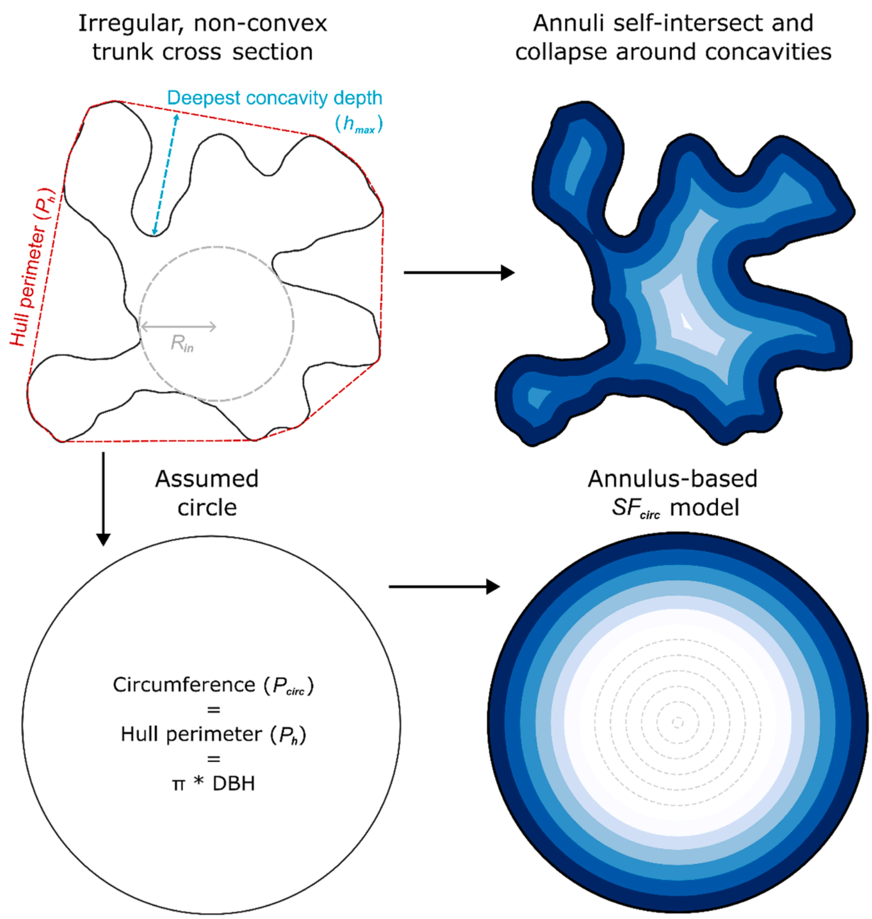

Fig. 3. Left: a non-convex *Pisonia grandis* trunk cross section and its assumed circle. The convex hull perimeter P_h is displayed with a red dashed line; the circle's circumference $P_{circ} = P_h$. On the right are both shapes eroded into nested annuli of equal thickness. The largest possible inscribed circle radius (R_{in}) is displayed in the trunk cross section; annuli with depths beyond R_{in} are displayed in the SF_{circ} model as grey dashed lines. The deepest concavity depth (h_{max}) is also displayed for reference.

than those of the assumed circle, leading to an **underestimation** of sap flow at these depths by SF_{circ}.

2. Drawing nested, constant-thickness annuli on irregular or non-convex shapes results in self-intersections that collapse annular areas when $r > r_{steiner}$. Beyond $r_{steiner}$, annular areas are smaller than those of the assumed circle (Fig. 4a), leading to **overestimation** of sap flow at these depths by SF_{circ}.
3. On an irregular cross section, the deepest annulus is only as deep as the incircle radius (r_{in}). For relative depths beyond r_{in}, annular areas are 0, leading to **overestimation** of sap flow at these depths by SF_{circ}.

3. Methods

3.1. Digitizing trunk cross sections

33 *Pisonia grandis* trees were haphazardly selected from Reiono and Tahuna Iti islets of Teti'aroa Atoll, French Polynesia (17°S 149.55°W). The sampled trees featured a wide range of DBHs and trunk forms.

To create digital representations of their trunk cross sections, we created trunk casts at 1.3 m height using 1 mm electrical wire (Ngomanda et al., 2012). Multiple lengths of wire were used on each tree and reassembled atop a flat surface with a printed regular grid of 4 cm^2 cells before being photographed from above.

We then orthorectified each image using the Georeferencer tool in QGIS 3.42.3. At least 9 control points were placed on visible grid points in each image and used to perform a thin plate spline transformation, correcting distortions in the wire cast photos.

Vectorized polygon representations of each orthorectified cross section (Fig. 5) were created using the Raster Tracer version 0.3.3 QGIS plug-in (Kondratyev, 2023). The resulting polygons were then re-sampled with 2 mm spacing along the boundary to ensure comparable scale relationships for all trees and smoothed slightly with Chaikin's algorithm (iterations = 1, offset = 0.5) to remove noise from the raster tracing (Chaikin, 1974).

Geometric properties were derived from these polygons and their assumed circles ($R_{circ} = P_h / 2\pi$) using the lwgeom (Pebesma, 2025) and sf (Pebesma, 2018; Pebesma and Bivand, 2023) packages in R 4.5.0 (R Core Team, 2025).

3.2. Spatial estimation of reference sap flow (SF_{ref})

In lieu of transpiration validation data, we compare integral-based *SF* estimates to reference *SF* (SF_{ref}) estimates modeled spatially from the trunk cross sections. By applying sap flux distributions to spatial erosions of these cross sections, SF_{ref} represents the theoretical *SF* that results from assuming negligible azimuthal variation in sap flux density and that radial sap flux profiles are measured perpendicularly to the trunk perimeter. These assumptions, though significant, are consistent with standard sap flow measurement practices (Komatsu et al., 2017).

While Eqs. (1)-(3) may be used with any $J_s(r)$ distribution, we follow Caylor & Dragoni (2009) and model the radial variability of sap flux density with a beta distribution. Beta distributions can flexibly model unimodal distributions using two shape parameters, making them a good candidate for approximating the sap flux profiles commonly found

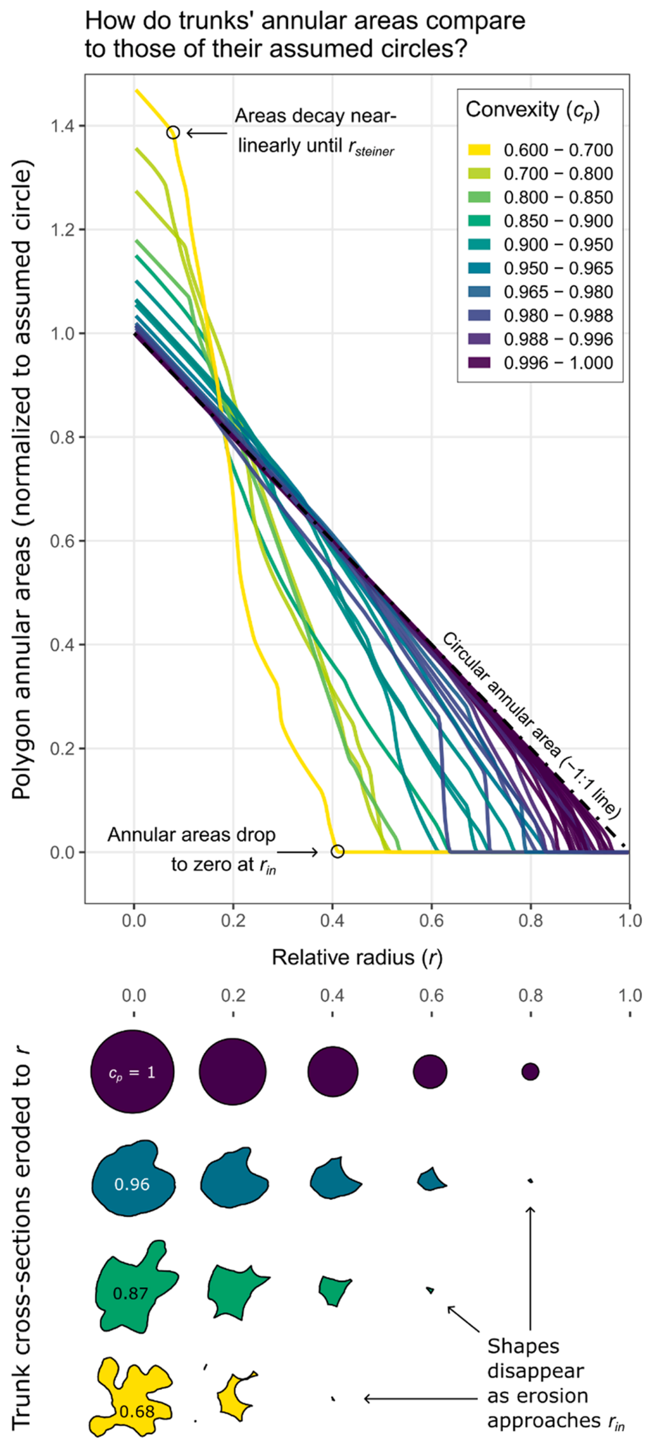

Fig. 4. a. Plots of 33 trunks' annular areas as functions of relative depth (dimensionless distance from the cambium at $r = 0$ to R_{circ} at $r = 1$). Annular area is normalized to the area of the outermost annulus of each trunk's assumed circle. The black dashed −1:1 line represents relative annular areas for a perfect circle. Each data series represents one tree, with colors displaying that tree's convexity (c_p). Each function's y-intercept equals the inverse of c_p, and the initial approximately linear slope equals negative c_p until $r_{steiner}$ is reached. The circular assumption underestimates annular areas until the function crosses the −1:1 line, at which point it overestimates annular areas. Annular areas collapse to 0 once the inscribed circle radius (r_{in}) is reached. b. Selected trunk cross sections and a perfect circle eroded to progressively greater values of r, demonstrating the total collapse of the polygons after r_{in}. c_p is reported for each cross section.

in dicot trees (Link et al., 2020). We adopt the reparameterization used by Link et al. (2020) to define the beta distribution using shape parameters $\mu = \alpha/(\alpha+\beta)$ (the mean relative depth of the distribution) and $K = \alpha+\beta$ (a concentration parameter describing the narrowness of the distribution's peak)(Ferrari and Cribari-Neto, 2004).

SF_{ref} was calculated for a trunk shape by incrementally eroding the polygon (Minkowski subtraction) using the st_buffer function of R package sf (Pebesma, 2018; Pebesma and Bivand, 2023). We use a constant offset increment (annulus width) of 0.5 mm, noting that increments of 0.3 and 0.7 mm produced negligible downstream differences in SF_{ref}. The area of each annulus was multiplied by the sap flux density midway between the inner and outer annulus boundaries; summing these annular sap flow values produced SF_{ref}.

3.3. Modeling potential SF_{circ} biases

To investigate the range of possible biases from applying the circular trunk assumption to trees with complex trunk morphologies, we simulated a grid of 24,120 beta distributions of sap flux density with 201 μ values linearly spaced across [0,1] and 120 K values log-spaced across [1,50].

For all 33 trunks, SF_{ref} was calculated for every (μ, K) combination using the spatial erosion method detailed above. SF_{circ}, $SF_{steiner}$, and SF_{corr} were estimated with Eqs. (5), (6), and (9), respectively. Sap flow bias ($Bias_{SF}$, Eq. (4)) was then plotted across the μ-K grid, revealing the range of biases possible for trees of diverse trunk convexities and sap flux profiles:

$$Bias_{SF} = \frac{SF_{circ/steiner/corr} - SF_{ref}}{SF_{ref}} \tag{4}$$

3.4. Correcting SF models using field measurements

3.4.1. Spatially estimating r_{in} and $r_{steiner}$ from digitized trunk cross sections

The relative inscribed circle radius, r_{in}, of each cross section was estimated as the total offset distance separating the outer boundary of its deepest eroded polygon from its original boundary.

We approximated the relative depth of topological change, $r_{steiner}$, as the relative depth at which the measured dimensionless annular area of a trunk cross section diverges from the annular areas predicted by Steiner's formulae (Eq. (A17)) by 0.02 units—an arbitrary threshold that appeared to place $r_{steiner}$ accurately across the wide variety of trunk shapes in our sample (Figure S4). A sensitivity analysis found that adjusting this threshold by 0.01 in either direction changed $_{SFcorr}$ estimates by <1% in all 33 trunks (see Supplement 6).

3.4.2. Deepest concavity depth (h_{max}) and DBH-normalized h_{rel}

To facilitate the application of SF_{corr} to new study systems, we set out to build predictive models of r_{in} and $r_{steiner}$ using only measurements that are relatively easy to collect in the field. In addition to perimeter and convex hull perimeter (by way of DBH), we evaluated the predictive power of the deepest concavity depth (h_{max}). h_{max} is the greatest exterior distance between the trunk and its convex hull as measured perpendicularly inward from the hull (Fig. 3), meaning it can be measured with a ruler while a DBH tape is pulled taught around the trunk.

We hypothesized that the deepest concavity depth would complement perimeter convexity by encoding information on a trunk's distribution of concavity—a larger h_{max} suggests the trunk features fewer, larger concavities while a smaller h_{max} indicates the trunk features more, smaller concavities. We divide h_{max} by DBH to create the dimensionless h_{rel}.

3.4.3. Predicting r_{in} and $r_{steiner}$ from field measurements

We tested linear and beta (with logit link function) regression models predicting r_{in} and $r_{steiner}$ from c_p and h_{rel}. These dimensionless metrics make the models sensitive to a trunk's shape rather than its overall size.

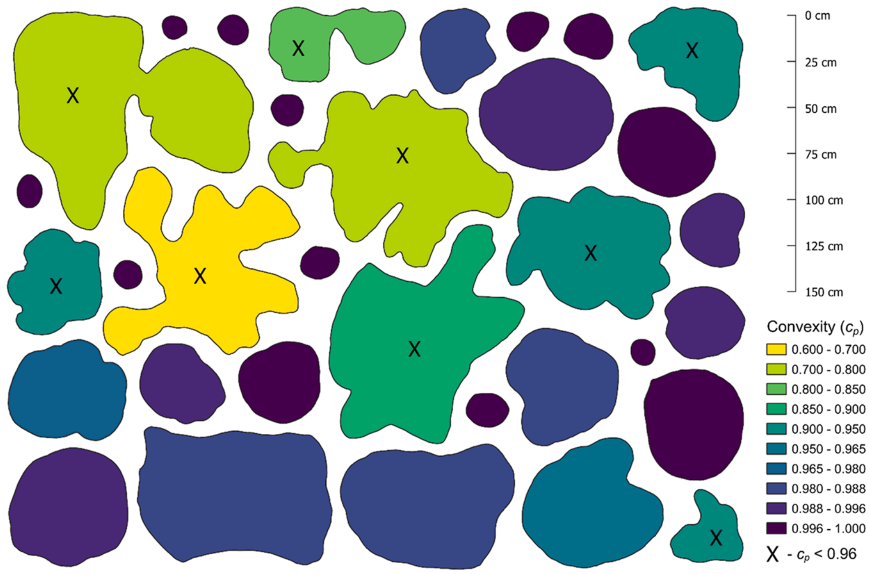

Fig. 5. 33 *Pisonia* trunk shapes photographed from wire casts, orthorectified, and resampled with 2 mm-spaced points. Colors indicate perimeter convexity (c_p). Shapes marked with an "X" feature $c_p < 0.96$, the proposed threshold above which SF bias is typically within ±5%.

In this way, the model should generalize more effectively to other tree species.

Linear and beta regressions were performed using the lm function and betareg package (Cribari-Neto and Zeileis, 2010) in R, respectively. Linear regressions used logit-transformed dependent variables to ensure predictions in (0,1). Evaluated models included independent variable transformations (none, ln, logit); 10-fold cross-validated RMSE was used to select the most accurate model family, and AIC corrected for small sample sizes (AICc) was used for within-family model comparison. Models with the lowest AICc were deemed the most parsimonious unless a model with fewer parameters produced an AICc within 2.0 of the lowest AICc.

3.5. Tree-level biases of SF_{circ} in Pisonia grandis

We calculated SF_{ref}, SF_{circ}, $SF_{steiner}$, and SF_{corr} for 33 *Pisonia grandis* trees using in-situ sap flux density measurements to demonstrate the magnitude of the assumed circle bias, and our ability to correct it, in real trees.

Sap flux profiles were not conserved across tree sizes. Rather, the total width of active sapwood was found to vary nonlinearly with DBH (Figure S1), and the shape of the sap flux profile within this active depth range was relatively stable across tree sizes (Figure S2).

In light of this observation, no global sap flux profile could be applied to all trees using relative depths, nor could any sap flux profile be applied to all trees using absolute depths (as would be possible if the depth of active sapwood was constant across tree sizes). We thus reparametrized SF_{ref}, SF_{circ}, $SF_{steiner}$, and SF_{corr} to use a beta distribution modeling sap flux density within the active sapwood only (see Section 3.5.3).

3.5.1. Sap flux density measurements

15 of the 33 *Pisonia* on Teti'aroa were instrumented with heat pulse velocity sap flow sensors following the design of Beslity et al. (2022). Probes were thermal epoxy-filled 16-gauge steel needles, 5 or 10 cm long, with four thermistors (3BT103R44T1A, North Star Sensors, Oceanside, CA) located at various depths within the probes. 5 s heat pulses dissipated 6 to 10 J every 30 min; temperatures were measured every half-second starting 10 s before the heat pulse and continuing for 100 s after. Probes were spaced 7 mm apart using a 1-inch-thick steel drill guide with the line of probes oriented parallel to the trunk.

Six months of sap flux data were collected between January and June 2024. 13 of the 15 instrumented trees were cored to estimate the radial profiles of wood density and moisture content in *Pisonia*, which were then used to estimate the thermal diffusivity of the wood surrounding every thermistor (Vandegehuchte and Steppe, 2012). Diffusivity increased slightly with depth and averaged about 0.0021 $cm^2\ s^{-1}$.

We then used the heat ratio method (Burgess et al., 2001) to estimate the sap flux density at each thermistor depth during every heat pulse. Sap flux density remained well within ±36 $cm^3\ cm^{-2}\ s^{-1}$, the heat ratio method's range limits for the observed diffusivity range (Forster, 2019), throughout the measurement period. To address probe misalignments, a zero-flow correction was implemented using a rolling 5-day mean of measurements between 2:00 and 4:30 am.

3.5.2. Sapwood depth measurements

Even with 10 cm probes, our sensors could only measure sap flux density at relatively shallow depths (i.e. at low r) on the largest trees. To better constrain our radial sap flux density profiles, we collected increment cores from 24 of the 33 sampled *Pisonia* and used the thermal imaging method of Gerchow et al. (2023) to estimate maximum sapwood depth (d_{sw}), i.e. the depth at which sap transport ceases. As recommended by Gerchow et al. (2023), a heat gun was used to enhance evaporation from the cores. The 24 cored individuals were then used to linearly regress d_{sw} against centered, log-transformed DBH with $r^2 = 0.36$ (Eq. S1.1). This model was then used to predict d_{sw} for all 33 trunks.

3.5.3. Modeling sap flow in Pisonia grandis

d_{sw} showed a nonlinear relationship with DBH, plateauing in larger trees (Figure S1). This finding mirrors the observation of Link et al. (2020) that taller tropical trees feature narrower sap flux density profiles that peak relatively closer to the cambium.

Consequently, no single radial sap flux density profile could be applied to the sampled *Pisonia*—the profile must be "compressed" on large trees and "stretched" on small trees. Unlike the simulations detailed in Section 3.3, in which sap flux profiles reached from the cambium to the theoretical center of the assumed circle, the sap flux profiles for *Pisonia* were defined using beta distributions between the cambium and d_{sw}.

To achieve this flexibility, we modeled sap flux density profiles in terms of z, the relative depth to d_{sw} (see Supplement 2). We thus reparametrized Eqs. (1) and (2) such that $r = pz$ and $dr = p\ dz$; in other words, p is a scalar relating the relative depth to d_{sw}, z, to the relative depth to R_{circ}, r:

$$SF_{circ} = 2\pi R_{circ}^2 p \int_0^1 (1 - pz) J_s(z)\, dz \tag{5}$$

$$SF_{steiner} = \frac{2\pi R_{circ}^2 p}{c_p} \int_0^1 (1 - c_p p z) J_s(z) dz \tag{6}$$

We model $J_s(z)$ with a beta distribution peaking toward the cambium ($\mu = 0.348$, $K = 3.66$; Figure S2). For any J_s distribution that integrates to 1 over [0,1], the closed forms[2] of Eqs. (5) and (6) are:

$$SF_{circ} = 2\pi R_{circ}^2 * p(1 - p\mu) \tag{7}$$

$$SF_{steiner} = \frac{2\pi R_{circ}^2 * p(1 - c_p p \mu)}{c_p} \tag{8}$$

SF_{corr} was estimated using the z-parametrized form[3] of Eq. (3), with $r_{steiner}$ and r_{in} predicted by the most parsimonious regression models from Section 3.4.3:

$$SF_{corr} = \frac{2\pi R_{circ}^2 p}{c_p} \left(\int_0^{\frac{r_{steiner}}{p}} (1 - c_p p z) J_s(z)\, dz + \int_{\frac{r_{steiner}}{p}}^{\frac{r_{in}}{p}} (1 - c_p r_{steiner}) \frac{r_{in} - pz}{r_{in} - r_{steiner}} J_s(z)\, dz \right) \tag{9}$$

SF_{ref} was generated using the erosion method detailed in Section 3.2 with the global $J_s(z)$ beta distribution for *Pisonia*. SF_{ref} uncertainty was propagated from d_{sw}(DBH) and the standard errors associated with μ and K for *Pisonia*'s $J_s(z)$ beta distribution (see Supplement 2).

For SF_{circ}, $SF_{steiner}$, and SF_{corr}, uncertainty from d_{sw}(DBH), $J_s(z)$, $r_{in}(c_p, h_{rel})$, and $r_{steiner}(c_p)$ were propagated wherever relevant, with beta regression variances arising from both coefficient standard errors and precision parameters.

4. Results

4.1. How much bias can result from the circular trunk assumption?

Simulations suggest large biases are possible when applying SF_{circ} to cross sections with low perimeter convexity and/or sap flux profiles concentrated in the inner trunk (large μ and, to a lesser extent, small K; see Fig. 6). The sign of the bias depends strongly on the mean (μ) of the beta distribution used to model $J_s(r)$; in extremely low-convexity trunks, a ~20% shift in μ could swing SF_{circ} bias from −25% to +50%.

4.2. Performance of two corrected sap flow models ($SF_{steiner}$ and SF_{corr})

Compared to SF_{circ}, $SF_{steiner}$ tends toward overestimating sap flow (Fig. 7a versus Fig. 6). Accuracy improvements over SF_{circ} are modest for most $J_s(r)$ distributions, and in some cases $SF_{steiner}$ performs worse than SF_{circ}. Meanwhile, SF_{corr} outperforms both SF_{circ} and $SF_{steiner}$ across a wide range of $J_s(r)$ profiles and trunk shapes, with most shallow-peaked profiles featuring bias <5% in all but the least convex trunks (Fig. 7b).

4.3. Predicting $r_{steiner}$ and r_{in} in non-convex trunk cross sections

In our sample of 33 trunk cross sections, we were able to predict the depth of topological collapse ($r_{steiner}$) from trunk convexity (c_p) with relatively low error (cross-validated RMSE of 0.076, or 7.6% of the distance from the cambium to R_{circ}). Contrary to our hypothesis, models with the relativized deepest concavity depth ($h_{rel} = h_{max}$ / DBH) included did not show meaningful improvements in performance (Table 1). Beta regressions proved more accurate than linear regressions. The model with the lowest AICc (Eqs. (10), (11)) is plotted in Fig. 8a.

$$\text{logit}(r_{steiner}) = 0.634 \times \text{logit}(c_p) - 2.885 \tag{10}$$

$$r_{steiner} = \frac{1}{1 + e^{2.885 - 0.634 \times \text{logit}(c_p)}} \tag{11}$$

Standard errors for the c_p coefficient and intercept are 0.040 and 0.205, respectively. The precision parameter was estimated at 20.728 ±7.257.

We were also able to predict the inscribed circle radius (r_{in}) with high accuracy from c_p and h_{rel} (cross-validated RMSE of 0.055, or 5.5% of the distance from the cambium to R_{circ}; see Table 2). Beta regressions again proved more accurate than linear regressions. The r_{in} model with the lowest AICc (Eqs. (12), (13)) is plotted in Fig. 8b.

$$\text{logit}(r_{in}) = 0.297 \times \text{logit}(c_p) - 1.767 \times h_{rel} + 0.303 \tag{12}$$

$$r_{in} = \frac{1}{1 + e^{1.767 \times (h_{max}/DBH) - 0.297 \times \text{logit}(c_p) - 0.303}} \tag{13}$$

Standard errors for the c_p coefficient, h_{rel} coefficient, and intercept are 0.049, 0.770, and 0.293, respectively. The precision parameter was estimated at 58.474±14.376.

In the case of r_{in}, including h_{rel} improved overall model accuracy only modestly, but significant improvements are visible at low c_p (Fig. 8b), so we believe h_{rel} should be included when modeling r_{in} in highly complex trunks. We provide the best performing c_p-only model in Supplement 3.

4.4. Tree-level SF biases in Pisonia grandis

SF_{circ} features strong negative biases relative to SF_{ref} in *Pisonia grandis*, with biases reaching −5% once trunk convexity drops below 0.96 and −25% once convexity reaches 0.68 (Fig. 9). SF_{circ}'s bias featured a strong positive linear correlation with trunk convexity (r^2= 0.961).

[2] The closed forms of SF_{circ} and $SF_{steiner}$ for $J_s(r)$ distributions spanning the entire range of depths from cambium to R_{circ} (as opposed to the range of depths from cambium to d_{sw}) can be produced by simply removing the p scalars from Eqs. (7) and (8), respectively. If SF_{circ} and $SF_{steiner}$ are modeled using $J_s(r)$ profiles not normalized to 1, the integral forms should be used instead of the closed forms.

[3] SF_{corr} lacks a closed form as clean as those of SF_{circ} and $SF_{steiner}$ for beta J_s distributions due to its use of incomplete distributions.

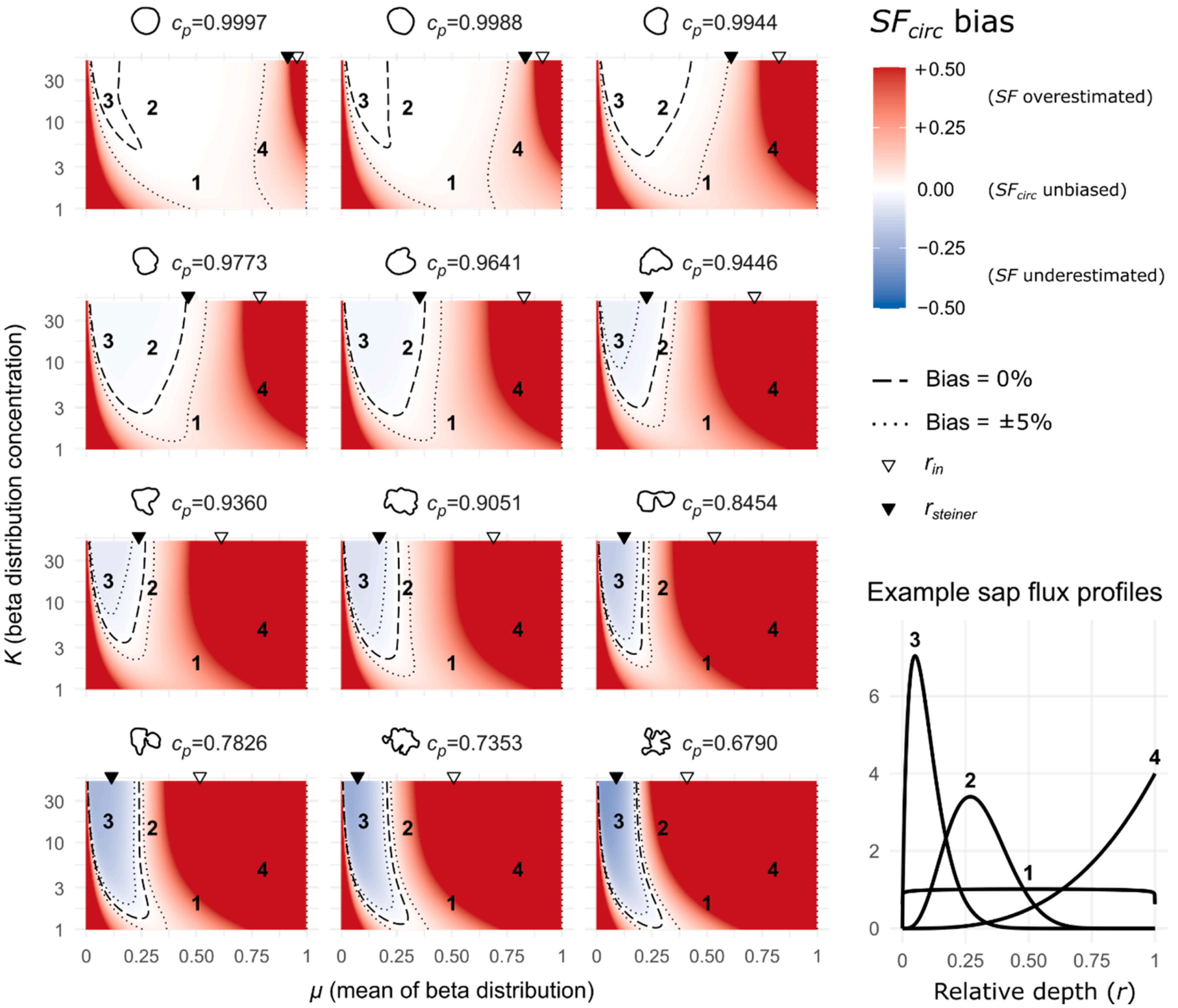

Fig. 6. Surface plots showing the SF_{circ} bias, $(SF_{circ}-SF_{ref})/SF_{ref}$, for beta $J_s(r)$ distributions with different μ and K parameters. The color scale is clipped to ±0.5 for interpretability, but every plot features some area in which SF_{circ} bias exceeds +0.5. The black dashed contour on each plot denotes the set of parameters for which the bias equals zero ($SF_{ref} = SF_{circ}$). Black dotted contours denote the parameter sets for which bias is ±5%. Note that μ is the mean of the beta distribution on the relative radial depth (r) scale. Each plot represents a different tree from our dataset (trunk outlines not to scale). Open triangles denote the relativized inscribed circle radius (r_{in}), or the relative depth beyond which annular areas are zero. Filled triangles represent $r_{steiner}$, the relative depth beyond which annular areas decay nonlinearly. Numbered labels represent the parameters of four example beta distributions displayed on the lower right.

$SF_{steiner}$'s biases are positive but smaller than SF_{circ}'s, reaching +6% once trunk convexity drops below 0.94 and +15% once convexity reaches 0.68. In effect, $SF_{steiner}$ slightly increased the range of trunk perimeter convexities for which SF can be estimated to within 5%.

SF_{corr} achieves the smallest overall biases, but with the widest confidence intervals due to the added uncertainty of modeling $r_{steiner}$ and r_{in} (Fig. 9). The only two trees for which SF_{corr} is biased beyond ±5% featured c_p values of 0.68 and 0.74 and h_{rel} values of 0.34 and 0.26, respectively, and bias for those two trees is still <7%. Importantly, the estimated confidence intervals for SF_{corr} bias nearly all include 0 (Fig. 9a).

5. Discussion

5.1. The circular trunk assumption can severely bias sap flow estimates

Our simulations show that in real trunk cross sections with low perimeter convexity, the circular trunk assumption can produce extremely biased sap flow estimates for typical sap flux profiles.

In Fig. 6, example sap flux profiles 2 and 3 are fairly typical of dicot trees (Berdanier et al., 2016; Link et al., 2020). Profile 1 represents a nearly flat sap flux profile more typical of monocots (Roupsard et al., 2006), but sometimes also observed in dicots (Link et al., 2020). If one takes the region of μ-K space represented by profiles 1–3 as the

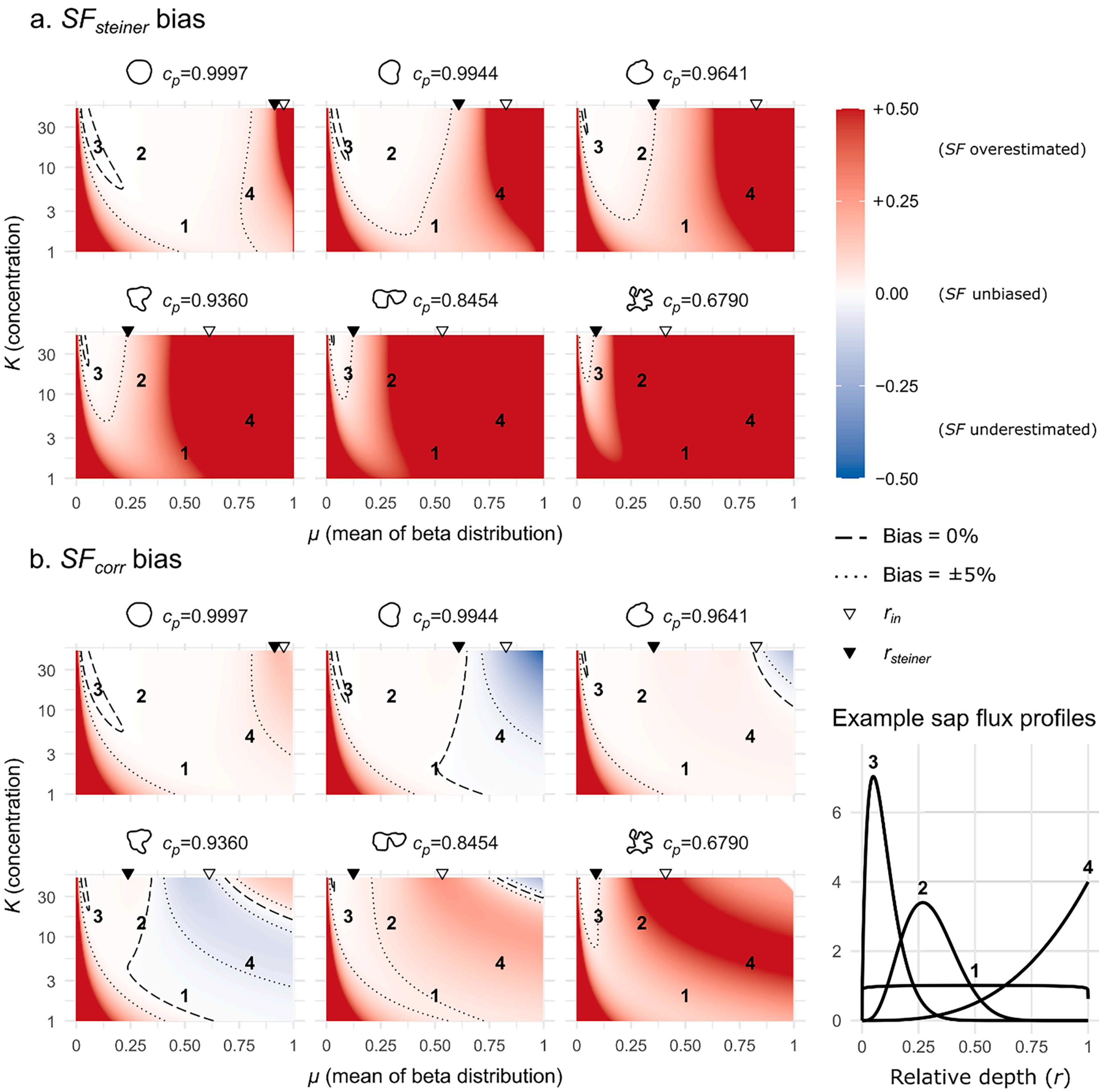

Fig. 7. As in Fig. 6, but for a. $SF_{steiner}$ and b. SF_{corr} in six selected cross sections.

Table 1
Cross-validation results for the five $r_{steiner}$ models with the lowest AICc.

Regression family	Terms	r^2	RMSE	MAE	AICc
Beta (logit-link)	$\mathrm{logit}(c_p)$	0.930	0.076	0.052	−73.8
Beta (logit-link)	$\mathrm{logit}(c_p) + \ln(h_{rel})$	0.933	0.075	0.051	−72.7
Beta (logit-link)	$\mathrm{logit}(c_p) + \mathrm{logit}(h_{rel})$	0.932	0.075	0.052	−72.3
Beta (logit-link)	$\mathrm{logit}(c_p) + h_{rel}$	0.928	0.077	0.052	−71.2
Beta (logit-link)	$\ln(h_{rel})$	0.863	0.106	0.086	−49.5

approximate range of plausible sap flux density profiles, the lowest-convexity trunk evaluated ($c_p = 0.68$) could be overestimated by >50% or underestimated by >25%.

For more convex trunks ($c_p > 0.96$), bias should be within 5% for most dicots, suggesting field measurements of both perimeter and convex hull perimeter (DBH*π) can immediately indicate the suitability of SF_{circ} for estimating sap flow.

Note that the theoretical lower limit for predicted sap flow bias, as defined as $(SF_{pred}-SF_{ref})/SF_{ref}$, equals $(c_p-1)/(1-c_p\mu)$ for distributions of sap flux density normalized to integrate to 1 over $r = [0,1]$ (see Appendix B). This limit may be useful to researchers evaluating the necessity of bias corrections.

5.2. Corrected sap flow models for irregular trunks

$SF_{steiner}$ and SF_{corr} achieved smaller biases than SF_{circ} for the 33 sampled *Pisonia* trunks (Fig. 9) and for large regions of the simulated sap flux profile space in Figs. 6 and 7.

While SF_{corr} is estimated with greater uncertainty than the other sap flow models due to its reliance on modeled $r_{steiner}$ and r_{in}, it is the only

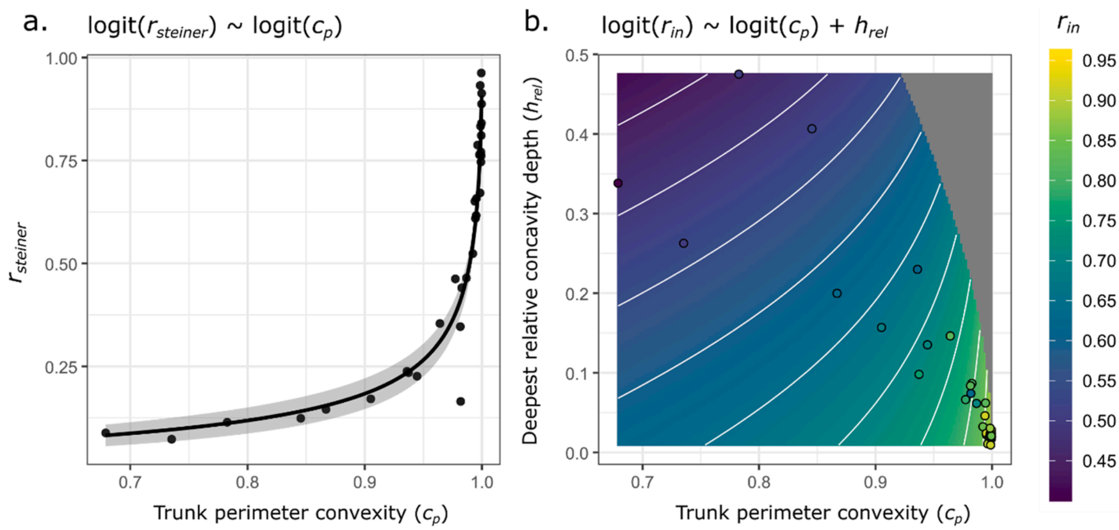

Fig. 8. a. Observed and predicted $r_{steiner}$ from the beta regression against logit-transformed convexity (c_p) in Eq. (11). Shaded region is the 95% confidence interval for the mean predicted $r_{steiner}$. b. The multiple beta regression surface of predicted r_{in} versus logit-transformed c_p and the DBH-normalized deepest concavity depth (h_{rel}) in Eq. (13). Observed r_{in} are plotted as points with the same color scale as predicted r_{in}. The grey region in the upper right is physically impossible space (see Supplement 4).

Table 2
Cross-validation results for the five r_{in} models with the lowest AICc.

Regression family	Terms	r^2	RMSE	MAE	AICc
Beta (logit-link)	logit(c_p) + h_{rel}	0.862	0.055	0.041	−100.6
Beta (logit-link)	logit(c_p) + logit(h_{rel})	0.867	0.054	0.041	−100.0
Beta (logit-link)	logit(c_p) + ln(h_{rel})	0.864	0.055	0.041	−99.3
Beta (logit-link)	logit(c_p)	0.851	0.057	0.047	−98.3
Beta (logit-link)	ln(c_p) + ln(h_{rel})	0.866	0.054	0.039	−96.8

model for which the 95% confidence intervals for bias versus SF_{ref} included 0 for nearly all sampled *Pisonia* (Fig. 9a). SF_{corr}'s slight trend toward overestimation stems from the use of a linear function to approximate a mostly concave-up relative annular area function between $r_{steiner}$ and r_{in}; this effect is magnified in less convex trunks (Fig. 4a).

The two *Pisonia* trunks for which SF_{corr} bias slightly exceeded 5% featured the lowest c_p values observed (0.68 and 0.74) as well as relatively high h_{rel} values (0.34 and 0.26). However, even greater h_{rel} values (0.47 and 0.41) were observed in two trunks with c_p values of 0.78 and 0.85, yet SF_{corr} biases for those trunks were modest (0.6% and 3.6%, respectively). Thus, even very high h_{rel} values seemed not to produce extreme SF_{corr} biases unless trunks also featured low perimeter convexities.

While SF_{corr} appears to be the most accurate sap flow model, its additional data requirement (h_{max}) must be kept in mind. For trees with sap flux concentrated near the cambium, the modest gains in accuracy over $SF_{steiner}$ may not be worthwhile. Additionally, SF_{corr}'s reliance on empirical relationships derived from *Pisonia* (Eqs. (10)–(13)) means it may not be valid for trees whose morphologies diverge significantly from those displayed in Fig. 5 (see Section 5.5).

5.3. Topological change depth ($r_{steiner}$) and inscribed circle radius (r_{in}) can be predicted from simple field measurements

To apply SF_{corr} to a real tree, both r_{in} and $r_{steiner}$ must be estimated. Eqs. (10) and (11) provide a strong predictive model of $r_{steiner}$ for non-convex trunk cross sections using only two field measurements (perimeter and DBH), while Eqs. (12) and (13) predict r_{in} with just one additional measurement (deepest concavity depth).

Contrary to our expectation, we found support for including deepest concavity depth as a predictor for r_{in} but not for $r_{steiner}$. And even for r_{in}, the improvement in model performance was minor (<0.2%, Table 2).

It is possible that the importance of deepest concavity depth for predicting $r_{steiner}$ would be observed in a larger selection of tree trunk morphologies, and it is a relatively simple measurement to add to field surveys. However, for 33 trunks with quite variable morphologies, trunk perimeter was the single most useful field measurement to pair with DBH to facilitate sap flow estimation. An empirical model predicting r_{in} without deepest concavity depth is available in Supplement 3, allowing SF_{corr} to be calculated without deepest concavity depth data.

It is possible that including other field measurements like cross sectional area could improve these empirical geometric models (see Supplement 5); here we have focused on measurements that are easy to acquire in the field.

5.4. Convexity and regularity in SF estimation

$SF_{steiner}$ and SF_{corr} both use trunk perimeter convexity (c_p) to correct SF_{circ} estimates for non-convex trunk cross sections. This approach has a sound theoretical basis in Steiner's formulae (Gray, 2004), but ignores the fact that even convex polygons depart from Steiner's formulae when eroded to sufficient depths if they are *irregular* (Appendix A.5).

A convex or near-convex trunk cross section could feature shallower $r_{steiner}$ and r_{in} than predicted by Eqs. (10)–(13) if it is significantly elongated in one direction, as in an ellipse. But the role of irregularity in drawing $r_{steiner}$ and r_{in} toward the cambium appears generally lesser than the role of concavities. Except in unlikely scenarios of significantly elongated, near-convex cross sections with very deep sap flow, $SF_{steiner}$, SF_{corr}, and the *Pisonia*-derived models for $r_{steiner}$ and r_{in} should remain useful.

5.5. Applicability to other species with irregular trunk morphologies

We cannot rule out the possibility that some species or individuals are morphologically different enough from *Pisonia grandis* to deviate from our proposed convexity threshold of 0.96 for applying SF_{circ}, or from the $r_{steiner}$ and r_{in} models we use to drive SF_{corr}. For instance, a highly elongated but nearly convex cross section may feature a convexity exceeding 0.96 but shallow $r_{steiner}$ and r_{in}, causing Eqs. (1) and (3) to overestimate SF.

In general, we suggest users should exercise caution when applying the *Pisonia*-derived $r_{steiner}$ and r_{in} models to trunks with a high degree of

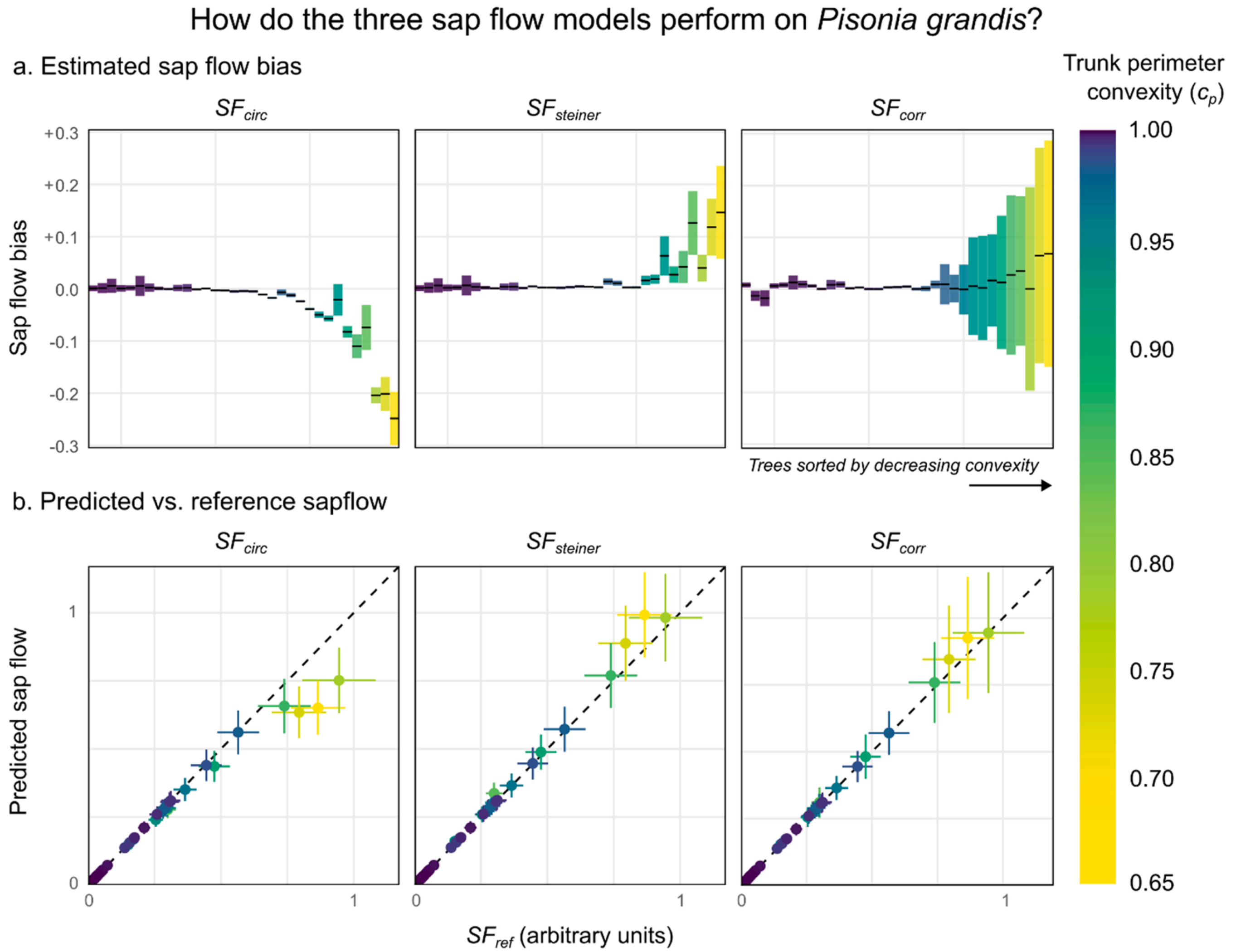

Fig. 9. a. Estimated biases of SF_{circ}, $SF_{steiner}$, and SF_{corr} versus SF_{ref} for 33 Pisonia grandis trees sorted in order of decreasing convexity (c_p). Colored bars are 95% confidence intervals. b. SF predicted by the three models versus SF_{ref} for the same 33 trees; units are arbitrarily scaled but consistent across axes. Error bars represent 95% confidence intervals calculated independently for each axis. The black dashed line represents perfect predictive accuracy (1:1).

irregularity but relatively high convexity (see Section 5.4, Appendix A.5), as in a near-elliptical trunk cross section, and to trunks with extremely long and thin buttresses whose $r_{steiner}$ and r_{in} may be shallower than predicted by Eqs. (10)–(13). Both $r_{steiner}$ and r_{in} were significantly overestimated for an almost rectangular trunk cross section with abnormally high irregularity for its level of convexity (outliers visible in Fig. 8; the trunk is visible in Fig. 5, second from left in the bottom row).

However, we note that our sample of 33 *Pisonia* trunks included a wide diversity of forms, including near-circular cross sections, star-shaped buttresses, large lobes connected by thin isthmuses, and sharp-cornered polygons (Fig. 5). Although some trunks may deviate from these relationships derived from one species growing on one atoll, the strength of the relationships across diverse trunk shapes suggests that they can be applied to other species with careful consideration.

If there are doubts as to whether the aforementioned relationships are applicable to a particular species—one with extremely thin and long root buttresses, for instance (Newbery et al., 2009)—this paper has also provided a workflow by which new $r_{steiner}$ and r_{in} relationships could be parameterized from a sample set before being deployed broadly to a larger population of the species. $SF_{steiner}$ may also provide accurate estimates of sap flow without relying on *Pisonia*-based empirical relationships if sap flux is demonstrably shallow relative to the diameter of the tree.

5.6. Sensitivity to measurement methods

When collecting perimeter and DBH data in the field for the purposes of quantifying trunk perimeter convexity, care must be taken to draw the taut diameter tape and flexible perimeter tape as straight as possible at precisely the same height on the tree. At our convexity threshold of 0.96, a trunk with a 31.8 cm DBH would have a perimeter of 100 cm and a convex hull perimeter of 96 cm. While a 4 cm difference is certainly detectable, it is of the same magnitude as errors that could stem from crooked or mislocated tape measurements.

To remain consistent with the assumptions of this study, all "radial" measurements (d_{sw}, J_s) should be considered locally perpendicular to the trunk's exterior and azimuthally invariant. This interpretation is consistent with the typical installation method of sap flow sensor probes and with recommended sampling strategies (Komatsu et al., 2017), though the consistency of radial sap flux density profiles in tree buttresses has yet to be rigorously tested. Further research into the azimuthal variability of sap flux in irregular trunks and the integration of this variability into the proposed trunk irregularity corrections is needed.

If our morphometric erosion protocol is used to model SF_{ref} (see Section 3.2), attention must also be paid to the method of trunk digitization. We recommend resampling digitized polygons with 2 mm or similar point spacing because inconsistent point densities could bias the computation of perimeter.

6. Conclusions

We recommend researchers follow this workflow to properly address SF upscaling in irregular or buttressed tree trunks (Fig. 1):

1. For irregularly shaped tree trunks, measure cross-sectional perimeter (P_0) as well as hull perimeter (P_h) at the same height as the sap flow sensor (if this height is 1.3 m, measuring P_h is equivalent to measuring DBH).

2. Estimate sapwood depth (d_{sw}) from increment cores or sap flow sensor data. Orient cores and sap flow probes perpendicular to the bark to remain consistent with this study's assumptions.

3. Calculate perimeter convexity ($c_p = (\text{DBH}^*\pi)/P_0$):

   a. If $c_p \geq 0.96$, use SF_{circ} (probably within ±5% of true sap flow); go to Step 5.
   b. If $c_p < 0.96$, go to Step 4.

4. Estimate $r_{steiner}$ from c_p (Eq. (10)):

   a. If sap flux only occurs shallower than $r_{steiner}$, use $SF_{steiner}$; go to Step 5.
   b. If sap flux may occur beyond $r_{steiner}$, measure deepest concavity depth (h_{max}) in the field, estimate r_{in} (Eq. (12)), and use SF_{corr}; go to Step 5.

5. If d_{sw} scales linearly with diameter, or if trunk diameter variations are not relevant to the study, use relative radius-parametrized SF models:

   a. SF_{circ}: Eq. (1)
   b. $SF_{steiner}$: Eq. (2)
   c. SF_{corr}: Eq. (3)

6. If d_{sw} scales nonlinearly with diameter, measure or model d_{sw} for each individual and use relative sapwood depth-parametrized SF models:

   a. SF_{circ}: Eq. (5)
   b. $SF_{steiner}$: Eq. (6)
   c. SF_{corr}: Eq. (9)

If trunk cross sections deviate significantly from the range of morphologies present in Fig. 5 (e.g. extremely thin buttresses or elongated high-convexity shapes), Eqs. (10)–(13) may not be valid. The convexity threshold of 0.96 may also fail to constrain SF_{circ} bias to ±5%. In these cases, the non-empirical $SF_{steiner}$ model may still be used if sap flux is concentrated at shallow depths. Otherwise, consider digitizing trunk cross sections and spatially estimating SF_{ref} as in Section 3.2.

Alongside this study we are providing an R package, "sapscaleR", that allows users to generate SF_{circ}, $SF_{steiner}$, and SF_{corr} from specified sap flux profiles and trunk measurements. The package can be downloaded at https://github.com/m1burnett/sapscaleR, or from the permanent Dryad repository that includes the data and code used in this paper (https://doi.org/10.5061/dryad.x0k6djj0n).

Funding sources

Fieldwork was supported by a Faculty Research Grant awarded by the Academic Senate of the University of California, Santa Barbara to LDLA, as well as a Schmidt Family Foundation Research Accelerator Award and an award from the Benioff Scholars Program in Applied Environmental Science, both to MWB. MWB was further supported by the NASA FINESST program (80NSSC24K0018).

CRediT authorship contribution statement

Michael W. Burnett: Conceptualization, Data curation, Formal analysis, Funding acquisition, Investigation, Methodology, Project administration, Resources, Software, Validation, Visualization, Writing – original draft. **Rayna Ruggeri:** Data curation, Investigation, Methodology, Resources. **Kelly K. Caylor:** Conceptualization, Formal analysis, Investigation, Supervision, Writing – review & editing. **Hillary S. Young:** Conceptualization, Investigation, Supervision, Writing – review & editing. **Leander D.L. Anderegg:** Conceptualization, Formal analysis, Investigation, Methodology, Supervision, Writing – review & editing.

Declaration of competing interest

The authors declare that they have no known competing financial interests or personal relationships that could have appeared to influence the work reported in this paper.

Acknowledgements

We gratefully acknowledge Joan Robson, Vairupe Huioutu Pater, Temakehu Murphy, Heimata Chenu, Tihoni Maire, and the rest of the staff of the Teti'aroa Society and The Brando for their support of this research. Rangers Tuterai Apuarii, Lusiano Kolokilagi, and Manea Brando were instrumental in facilitating access to field sites. We also thank Justin Beslity and Lincoln Satterthwaite for their help with sensor and equipment design. Michael Bliss-Schryer, Charlie Braman, Irina Roybal, Alex Fischer, and Talula Wilmot assisted with field data collection, and Malkin Gerchow generously assisted with the analysis of increment cores.

Supplementary materials

Supplementary material associated with this article can be found, in the online version, at doi:10.1016/j.agrformet.2026.111357.

Appendix A: Deriving SF_{circ}, $SF_{steiner}$, and SF_{corr}

Consider a perfectly circular trunk cross section with radius R_{circ}. Its circumference P_0 is:

$$P_0 = 2\pi R_{circ} \tag{A1}$$

Let t denote an absolute inward radial distance such that $R(t)$, $A(t)$, and $P(t)$ equal the radius, area, and circumference of the circle obtained by morphologically eroding the original circle by offset distance t. Let $J_s(t)$ be the sap flux density for depth t.

A.1. Steiner's formulae and thin annuli

Steiner's formulae for parallel convex sets present A(t) and P(t) as Eqs. (A2) and (A3), respectively (Gray, 2004). These formulae are exact for circles:

$$A(t) = A_0 - P_0 t + \pi t^2 \tag{A2}$$

$$P(t) = P_0 - 2\pi t \tag{A3}$$

If circle A is the original circle eroded to depth t, and circle B is the original circle eroded to depth $t+\Delta$, subtracting B from A would produce an annulus of thickness Δ and outer edge depth t. Its area, $a(t)$, can be calculated for any convex polygon with Eq. (A4):

$$a(t) = A(t) - A(t+\Delta) = P(t)\Delta - \pi\Delta^2 \tag{A4}$$

A.2. Computing SF across absolute radial depths

$$SF \approx \sum_{t\in\{0,\Delta,2\Delta,\ldots\}} J_s(t)a(t) \tag{A5}$$

This is a Riemann sum approximating the following integral:

$$SF = \frac{1}{\Delta}\int_0^{R_{circ}} J_s(t)a(t)dt \tag{A6}$$

Substituting Eq. (A4) into Eq. (A6):

$$SF = \int_0^{R_{circ}} J_s(t)\frac{P(t)\Delta - \pi\Delta^2}{\Delta}dt = \int_0^{R_{circ}} J_s(t)(P(t) - \pi\Delta)dt \tag{A7}$$

As Δ approaches 0, Eq. (A7) reduces to:

$$SF \approx \int_0^{R_{circ}} J_s(t)P(t)dt \tag{A8}$$

Intuitively, for tiny Δ, the Δ^2 term in Eq. (A4) becomes negligible, so annulus area can be approximated by the perimeter times Δ. Δ can also be written as dt, so Eq. (A8) is simply multiplying annulus areas by their corresponding sap flux densities, as in Eq. (A5).

A.3. Computing SF across relative radial depths

Now we adopt the terminology of (Link et al., 2020), who define r as the relative radial depth from the cambium (at $r = 0$) to the center of the trunk (at $r = 1$):

$$r = \frac{t}{R_{circ}},\ r \in [0, 1] \tag{A9}$$

In terms of relative depth r, Eq. (A8) becomes:

$$SF = R_{circ}\int_0^1 J_s(r)P(r * R_{circ})dr \tag{A10}$$

Plugging in Eq. (A3) yields:

$$SF = R_{circ}\int_0^1 J_s(r)(P_0 - 2\pi r R_{circ})dr \tag{A11}$$

And for a circle, $P_0 = 2\pi R_{circ}$:

$$SF_{circ} = R_{circ}\int_0^1 J_s(r)(2\pi R_{circ} - 2\pi r R_{circ})dr = 2\pi {R_{circ}}^2\int_0^1 J_s(r)(1-r)dr \tag{A12}$$

Eqs. A12 is the time-invariant form of Eq. (A5) in (Link et al., 2020). Within the integrand, $J_s(r)$ is now multiplied by a *dimensionless annulus area density* function—in a circle's case, $(1-r)$—while the $2\pi {R_{circ}}^2$ prefactor provides the area scaling now absent from the integrand.

A.4. Dimensionless annular area density, g(r)

We term this dimensionless annulus area density function $g(r)$, and it represents the area of the annulus at relative depth r divided by the area of the outermost annulus of equal width:

$$g(r) = \frac{a(r)}{a(0)} \tag{A13}$$

Plugging Eq. (A4) into Eq. (A13), we find that for small Δ, $g(r)$ can be approximated by a ratio of perimeters:

$$g(r) = \frac{P(r * R_{circ})\Delta - \pi\Delta^2}{P_0\Delta - \pi\Delta^2} \approx \frac{P(r * R_{circ})}{P_0} \tag{A14}$$

In the special case of a circle, using Eq. (A3) in Eq. (A14) verifies the dimensionless area slope used in Eq. (A12):

$$g_{circ}(r) \approx \frac{P_0 - 2\pi(r * R_{circ})}{P_0} = \frac{P_0 - rP_0}{P_0} = 1 - r \tag{A15}$$

Thus for a perfect circle, the relative annular area decreases linearly from 1 to 0 as r increases from 0 to 1. But as we will see below, $g(r)$ differs for irregular and non-convex shapes.

A.5. Applying SF_{circ} to an irregular, convex trunk cross section

Now consider a trunk cross section that is an irregular, but still convex, polygon. This cross section has perimeter P_0 and an assumed circle of radius R_{circ} whose circumference equals P_0 (Fig. A1). Crucially, relative radial depth (r) will continue to be calculated in terms of R_{circ}.

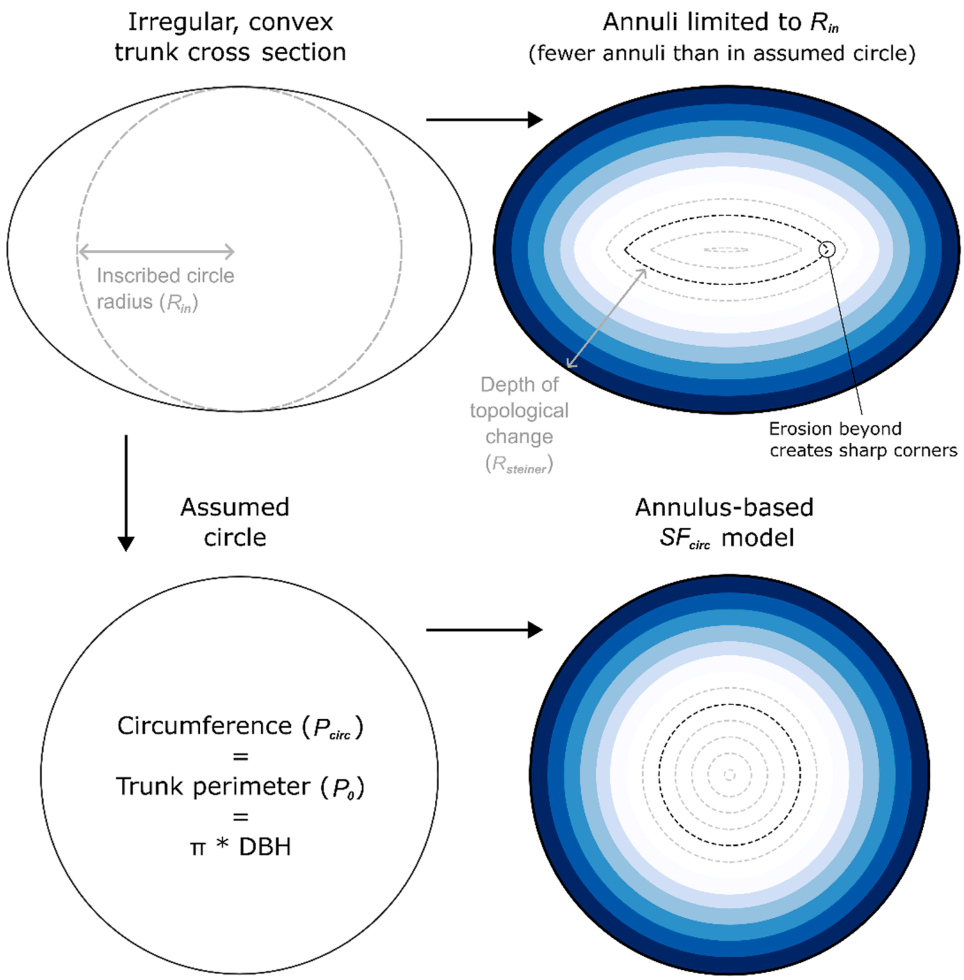

Fig. A1. A theoretical irregular, convex trunk cross section (in this case an ellipse) and its annular SF approximation compared to that of its assumed circle. The circle's circumference (P_{circ}) equals the elliptical trunk's perimeter (P_0), which is equal to its hull perimeter because it is convex. All annuli possess equal thickness in both the ellipse and circle. The radius of the largest possible inscribed circle (R_{in}) represents the maximum erosion depth possible for a shape (note the ellipse possesses fewer annuli than the circle; no annuli are possible beyond R_{in}, which must be less than R_{circ}). The approximate depth of topological collapse ($R_{steiner}$) is represented by the black dashed annulus boundary in the upper right diagram; the annulus at the same absolute depth is depicted in black in the SF_{circ} model for reference despite no topological collapse occurring in a perfect circle. Erosion beyond $R_{steiner}$ results in topological changes like new sharp corners, causing eroded annulus areas and perimeters to diverge from Steiner's formulae.

In keeping with our assumption of azimuthally invariant J_s profiles (which we treat as representing the inward normal from any point on the cambium), we continue with our constant-width annulus-based model of J_s variability. But when eroding an irregular polygon in this manner, it will cease to exist before t reaches R_{circ}, meaning $a(r)$ and $g(r)$ will abruptly drop to 0 at some r between 0 and 1.

This total annular area collapse occurs once t equals the radius of the largest circle that can possibly be inscribed within the polygon (R_{in}). Functionally, R_{in} is the shortest distance between the original polygon boundary and the smallest polygon possible from a constant-offset erosion.

But even before the constant-offset erosion reaches R_{in}, an important topological process is visible in the ellipses of Fig. A1. Once the erosion reaches the black dashed annulus boundary, sharp corners develop in the previously smooth boundaries, causing a topological change and divergence from Steiner's formulae (Eqs. (A2), (A3)) .[4] We term this depth $R_{steiner}$, or $r_{steiner} \in (0,1)$ in its relativized form.

Eq. (A14) is therefore valid for any convex polygon, but only for $t \leq R_{steiner}$ (or $r \leq r_{steiner}$, where $r_{steiner}$ is $R_{steiner}/R_{circ}$). So **the SF_{circ} model in Eq. (A12) will produce reasonable estimates of SF in a convex, irregular polygon as long as $J_s(r)$ is insignificant at $r > r_{steiner}$.** Fortunately, for most plausible trunk cross sections that are irregular but totally convex, $r_{steiner}$ will be relatively deep.

A.6. Correcting SF_{circ} for non-convex trunk cross sections

Now consider a non-convex polygon representing a trunk cross section (Fig. 3). The true perimeter of this polygon is P_0. The polygon's assumed circle features radius R_{circ} and circumference $P_{circ} = P_h$, as would be measured by a taut diameter tape.

Here we introduce perimeter convexity (c_p), which quantifies the degree to which a shape's perimeter departs from that of its convex hull (Zunic and Rosin, 2004):

$$c_p = \frac{P_h}{P_0} \tag{A16}$$

To calculate SF for the non-convex polygon, the slope of $g(r)$ must be modified. We define $g_{steiner}(r)$ as the dimensionless annular area density of a non-convex polygon. Recall that r is defined using the shape's assumed circle, so regardless of the actual nature of the trunk cross section, $2\pi R_{circ}$ equals P_h:

$$g_{steiner}(r) \approx \frac{P_0 - 2\pi(r * R_{circ})}{P_0} = \frac{P_0 - rP_h}{P_0} = 1 - r\frac{P_h}{P_0} = 1 - c_p r \tag{A17}$$

Essentially, c_p corrects the slope of $g(r)$, allowing $g_{steiner}(r)$ to approximate the relative areas of non-convex annuli.

But in addition to correcting the slope of $g(r)$, the prefactor in Eq. (A12) must be modified to properly scale sap flow across the non-convex trunk cross section. To derive this prefactor, $g(r)$ can be written explicitly into the integrand of Eq. (A10) by dividing by P_0:

$$SF = R_{circ}\int_0^1 J_s(r)P(r * R_{circ})dr = P_0 R_{circ}\int_0^1 J_s(r)\underbrace{\frac{P(r * R_{circ})}{P_0}}_{g(r)}dr \tag{A18}$$

Substituting Eq. (A17) into Eq. (A18) yields a corrected formula for estimating SF in non-convex trunk cross sections. We call this estimate $SF_{steiner}$ because it originates from Steiner's formulae (Eqs. (A2), (A3)):

$$SF_{steiner} = \frac{2\pi {R_{circ}}^2}{c_p}\int_0^1 (1 - c_p r)J_s(r)\,dr \tag{A19}$$

However, as was the case for irregular convex polygons, Steiner's formulae (and thus $g_{steiner}(r)$ in Eq. (A17)) are only valid in non-convex polygons for $r \leq r_{steiner}$, meaning Eq. (A19) **only provides useful estimates of SF when J_s is concentrated in the outer regions of the trunk.** This is true of many dicot trees, but with exceptions (Berdanier et al., 2016; Link et al., 2020).

While $SF_{steiner}$ is only accurate where $g(r)$ can be approximated by Eq. (A17) (i.e. for $r \leq r_{steiner}$), a more complete correction of SF_{circ} can be achieved with knowledge of both $r_{steiner}$ and r_{in}. Between these depths, $g(r)$ decreases monotonically to zero (Fig. 4). By assuming a linear decrease from $g(r_{steiner})$ to $g(r_{in})$=0, we can produce a model of $g(r)$ spanning $r \in (0,1)$, hereafter called $g_{corr}(r)$:

$$g_{corr}(r) = \begin{cases} 1 - c_p r, \ 0 < r \leq r_{steiner} \\ (1 - c_p r_{steiner})\dfrac{r_{in} - r}{r_{in} - r_{steiner}}, \ r_{steiner} < r < r_{in} \\ 0, \ r_{in} \leq r < 1 \end{cases} \tag{A20}$$

Accordingly, corrected sap flow (SF_{corr}) can be calculated using Eq. (A21):

$$SF_{corr} = \frac{2\pi {R_{circ}}^2}{c_p}\left(\int_0^{r_{steiner}} (1 - c_p r)J_s(r)\,dr + \int_{r_{steiner}}^{r_{in}} (1 - c_p r_{steiner})\frac{r_{in} - r}{r_{in} - r_{steiner}}J_s(r)\,dr\right) \tag{A21}$$

[4] Such topological change events occur at interior vertices of the polygon's medial axis (Dorado, 2009): If one imagines erosion as an inward-propagating wavefront or grass fire, the medial axis marks the points at which the wavefront's topology changes significantly (Blum, 1967). Before the wavefront reaches the axis, all annuli are locally parallel to their neighboring annuli and Steiner's formulae (Gray, 2004) are valid. Once the wavefront crosses it, either a wavefront segment will collapse to zero length or two non-adjacent wavefront segments will become tangent, invalidating Steiner's formulae. Even with a well-described trunk cross section, the computation of significant medial axis vertices is unstable (Attali et al., 2009; Chambers et al., 2022).

Appendix B: An upper bound on sap flow bias for normalized sap flux profiles

Imagine a non-convex polygon with area A_0, perimeter P_0, convex hull perimeter P_h, perimeter convexity $c_p = P_h/P$, and assumed circle radius $R_{circ} = P_h/(2\pi)$. For $t \leq R_{steiner}$, Steiner's formulae (Gray, 2004) provide the area of the eroded shape $A(t)$ as:

$$A(t) = A_0 - P_0 t + \pi t^2 \tag{B1}$$

Differentiating Eq. (B1) yields the rate of area loss per unit depth at depth t. This equation will naturally yield negative values; multiplying by -1 produces the annular area density per unit t:

$$-\frac{dA(t)}{dt} = P_0 - 2\pi t \tag{B2}$$

Near the boundary where t is approximately 0, the annular area $-dA(t)$ becomes approximately $P_0 * dt$ (original perimeter times annulus thickness). As the erosion moves inward and t increases, curvature reduces the available length at a rate of $2\pi t$.

In terms of relative depth $r = t/R_{circ}$ and $dt = R_{circ} dr$, annular area density per unit r is:

$$-\frac{dA(r)}{dr} = R_{circ}(P_0 - 2\pi r R_{circ}) \tag{B3}$$

And for the circle with circumference P_h,

$$-\frac{dA_{circ}(r)}{dr} = R_{circ}(P_h - 2\pi r R_{circ}) \tag{B4}$$

Now define $q(r)$ as the ratio between the shape's local annular area density and that of the assumed circle:

$$q(r) = -\frac{dA(r)}{dr} \Big/ -\frac{dA_{circ}(r)}{dr} = \frac{R_{circ}(P_0 - 2\pi r R_{circ})}{R_{circ}(P_h - 2\pi r R_{circ})} = \frac{1 - c_p r}{c_p(1 - r)} \tag{B5}$$

Note that in this non-convex polygon, Eq. (B1) is only valid for $r \leq r_{steiner}$. In reality, r will cross $r_{steiner}$ eventually and self-intersections will form, causing annular areas for the polygon (the numerator in $q(r)$) to fall below the line presented in Eq. (B5). Eq. (B5) can therefore be considered an upper bound for the $q(r)$ of any polygon.

This theoretical upper-bound $q(r)$ can be visualized in Fig. 4a: for any of the 33 polygons, the portion of the function to the left of the $r_{steiner}$ cusp shows the upper bound given in Eq. (B5), but every polygon's relativized annular area density eventually falls below its line's continuation.

Now consider the whole-tree SF_{circ} bias, which can be calculated as:

$$\frac{SF_{circ} - SF_{ref}}{SF_{ref}} = \frac{\int_0^1 (1-r) J_s(r) dr - \int_0^1 (1-r) J_s(r) q(r) dr}{\int_0^1 (1-r) J_s(r) q(r) dr} \tag{B6}$$

Maximizing $q(r)$ will minimize $(SF_{circ} - SF_{ref})/SF_{ref}$. Since Eq. (B5) provides an upper bound for $q(r)$, Eq. (B6) really provides a lower bound for SF bias:

$$Bias_{SF} \geq \frac{\int_0^1 (1-r) J_s(r) dr - \int_0^1 (1-r) J_s(r) q(r) dr}{\int_0^1 (1-r) J_s(r) q(r) dr} \tag{B7}$$

For any $J_s(r)$ distribution normalized to integrate to 1 from $r = 0$ to $r = 1$,

$$\int_0^1 (1-r) J_s(r) dr = 1 - \mu \tag{B8}$$

where μ is the mean of the distribution. Plugging this equivalency into the bias equation yields:

$$\begin{aligned} Bias_{SF} &\geq \frac{1 - \mu - \int_0^1 (1-r) J_s(r) \left(\frac{1 - c_p r}{c_p(1-r)}\right) dr}{\int_0^1 (1-r) J_s(r) \left(\frac{1 - c_p r}{c_p(1-r)}\right) dr} = \frac{1 - \mu - \int_0^1 J_s(r) \left(\frac{1 - c_p r}{c_p}\right) dr}{\int_0^1 J_s(r) \left(\frac{1 - c_p r}{c_p}\right) dr} \\ &= \frac{1 - \mu - \frac{1}{c_p} \int_0^1 J_s(r)(1 - c_p r) dr}{\frac{1}{c_p} \int_0^1 J_s(r)(1 - c_p r) dr} = \frac{1 - \mu - \frac{1}{c_p}(1 - c_p \mu)}{\frac{1}{c_p}(1 - c_p \mu)} = \frac{c_p - 1}{1 - c_p \mu} \end{aligned} \tag{B9}$$

For any polygon of given c_p and μ, $Bias_{SF}$ will never be lower (more negative) than the result of Eq. (B9). This lower bound may be useful to evaluate the necessity of bias corrections for a new tree with a known c_p and beta-shaped J_s profile. For c_p sufficiently close to 1 and/or μ sufficiently close to 0, worst-case overestimation may be relatively small (Fig. B1).

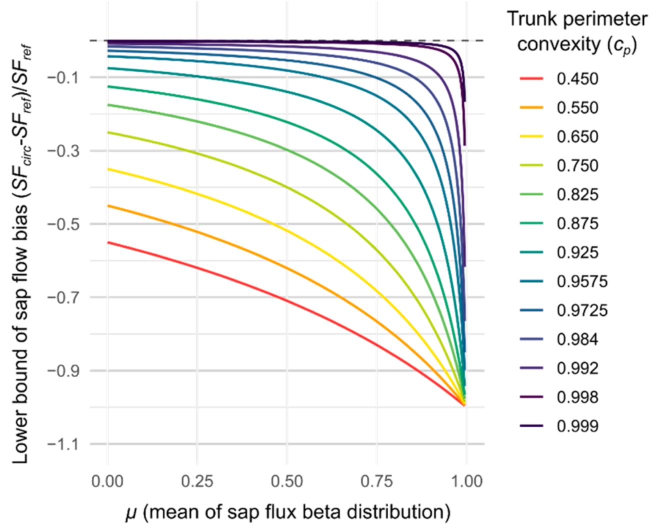

Fig. B1. Lower bounds of circular assumption sap flow bias for trunk cross sections of various c_p across the entire range of possible distribution means (μ), with 0 representing the cambium and 1 the assumed circle radius (R_{circ}).

Data availability

The data and scripts used in this study are available from Dryad (https://doi.org/10.5061/dryad.x0k6djj0n). We also provide an R package, sapscaleR, at https://github.com/m1burnett/sapscaleR.

References

Attali, D., Boissonnat, J.-D., Edelsbrunner, H., 2009. Stability and computation of medial axes—A State-of-the-art report. Mathematical Foundations of Scientific Visualization, Computer Graphics, and Massive Data Exploration. Springer, Berlin, Heidelberg, pp. 109–125. https://doi.org/10.1007/b106657_6.

Batianoff, G.N., 1999. Floristic, vegetation and shoreline changes on Masthead Island, Great Barrier Reef. Proc. R. Soc. Qld. 108, 1–11.

Berdanier, A.B., Miniat, C.F., Clark, J.S., 2016. Predictive models for radial sap flux variation in coniferous, diffuse-porous and ring-porous temperate trees. Tree Physiol. 36 (8), 932–941. https://doi.org/10.1093/treephys/tpw027.

Beslity, J., Shaw, S.B., Drake, J.E., Fridley, J., Stella, J.C., Stark, J., Singh, K., 2022. A low cost, low power sap flux device for distributed and intensive monitoring of tree transpiration. HardwareX 12, e00351. https://doi.org/10.1016/j.ohx.2022.e00351.

Blum, H., 1967. A transformation for extracting new descriptors of shape. In: Wathen-Dunn, W. (Ed.), Models For the Perception of Speech and Visual Form. MIT Press, pp. 362–380.

Burger, A.E., 2005. Dispersal and germination of seeds of *Pisonia grandis*, an Indo-Pacific tropical tree associated with insular seabird colonies. J. Trop. Ecol. 21 (3), 263–271. https://doi.org/10.1017/S0266467404002159.

Burgess, S.S.O., Adams, M.A., Turner, N.C., Beverly, C.R., Ong, C.K., Khan, A.A.H., Bleby, T.M., 2001. An improved heat pulse method to measure low and reverse rates of sap flow in woody plants. Tree Physiol. 21 (9), 589–598. https://doi.org/10.1093/treephys/21.9.589.

Burnett, M.W., French, R., Jones, B., Fischer, A., Holland, A., Roybal, I., White, T., Steibl, S., Anderegg, L.D.L., Young, H., Holmes, N.D., Wegmann, A., 2024. Satellite imagery reveals widespread coconut plantations on Pacific atolls. Environ. Res. Lett. 19 (12), 124095. https://doi.org/10.1088/1748-9326/ad8c66.

Caylor, K.K., Dragoni, D., 2009. Decoupling structural and environmental determinants of sap velocity: part I. Methodological development. Agric. For. Meteorol. 149 (3–4), 559–569. https://doi.org/10.1016/j.agrformet.2008.10.006.

Chaikin, G.M., 1974. An algorithm for high-speed curve generation. Comput. Graph. Image Process. 3, 346–349. https://doi.org/10.1016/0146-664X(74)90028-8.

Chambers, E., Fillmore, C., Stephenson, E., Wintraecken, M., 2022. A cautionary tale: burning the medial axis is unstable. LIPIcs 224 (66), 1–9. https://doi.org/10.4230/LIPICS.SOCG.2022.66.

Cribari-Neto, F., Zeileis, A., 2010. Beta regression in R. J. Stat. Softw. 34 (2), 1–24. https://doi.org/10.18637/jss.v034.i02.

Cribb, A.B., 1969. The *Pisonia*. Qld. Nat. 19 (4–6), 110–114.

Dean, C., Roxburgh, S., Mackey, B., 2003. Growth modelling of *Eucalyptus regnans* for carbon accounting at the landscape scale. In: Amaro, A., Reed, D., Soares, P. (Eds.), Modelling Forest Systems, 1. CABI Publishing, pp. 27–39.

Dorado, R., 2009. Medial axis of a planar region by offset self-intersections. Comput.-Aided Des. 41 (12), 1050–1059. https://doi.org/10.1016/j.cad.2009.08.005.

Edwards, W., Warwick, N., 1984. Transpiration from a kiwifruit vine as estimated by the heat pulse technique and Penman–Monteith equation. N. Z. J. Agric. Res. 27, 537–543. https://doi.org/10.1080/00288233.1984.10418016.

Edwards, W.R.N., Becker, P., Eermak, J., 1997. A unified nomenclature for sap flow measurements. Tree Physiol. 17 (1), 65–67. https://doi.org/10.1093/treephys/17.1.65.

Ferrari, S., Cribari-Neto, F., 2004. Beta regression for modelling rates and proportions. J. Appl. Stat. 31 (7), 799–815. https://doi.org/10.1080/0266476042000214501.

Forster, M.A., 2019. The dual method approach (DMA) resolves measurement range limitations of heat pulse velocity sap flow sensors. Forests 10 (1), 46. https://doi.org/10.3390/f10010046.

Gerchow, M., Marshall, J.D., Kühnhammer, K., Dubbert, M., Beyer, M., 2023. Thermal imaging of increment cores: a new method to estimate sapwood depth in trees. Trees 37 (2), 349–359. https://doi.org/10.1007/s00468-022-02352-7.

Gray, A., 2004. Steiner's formula. Tubes, 2nd ed. Birkhäuser Basel, pp. 209–229. https://doi.org/10.1007/978-3-0348-7966-8_10.

Green, S.R., Clothier, B.E., 1988. Water use of kiwifruit vines and apple trees by the heat-pulse technique. J. Exp. Bot. 39 (198), 115–123. https://doi.org/10.1093/jxb/39.1.115.

Hallé, F., Oldeman, R.A.A., Tomlinson, P.B., 1978. Tropical Trees and Forests: an Architectural Analysis. Springer-Verlag, Berlin, p. 441.

He, Z., Tang, Y., Deng, X., Cao, M., 2013. Buttress trees in a 20-hectare tropical dipterocarp rainforest in Xishuangbanna, SW China. J. Plant Ecol. 6 (2), 187–192. https://doi.org/10.1093/jpe/rts031.

Komatsu, H., Kume, T., Shinohara, Y., 2017. Optimal sap flux sensor allocation for stand transpiration estimates: a non-dimensional analysis. Ann. For. Sci. 74 (2), 38. https://doi.org/10.1007/s13595-017-0638-x.

Kondratyev, M., 2023. Raster Tracer (Version 0.3.3) [Python; QGIS plug-in]. https://github.com/mkondratyev85/raster_tracer/.

López-Bernal, Á., Alcántara, E., Testi, L., Villalobos, F.J., 2010. Spatial sap flow and xylem anatomical characteristics in olive trees under different irrigation regimes. Tree Physiol. 30 (12), 1536–1544. https://doi.org/10.1093/treephys/tpq095.

Link, R.M., Fuchs, S., Arias Aguilar, D., Leuschner, C., Castillo Ugalde, M., Valverde Otarola, J.C., Schuldt, B., 2020. Tree height predicts the shape of radial sap flow profiles of Costa-Rican tropical dry forest tree species. Agric. For. Meteorol. 287, 107913. https://doi.org/10.1016/j.agrformet.2020.107913.

Lu, P., Müller, W.J., Chacko, E.K., 2000. Spatial variations in xylem sap flux density in the trunk of orchard-grown, mature mango trees under changing soil water conditions. Tree Physiol. 20 (10), 683–692. https://doi.org/10.1093/treephys/20.10.683.

Marshall, D.C., 1958. Measurement of sap flow in conifers by heat transport. Plant Physiol. 33 (6), 385–396. https://doi.org/10.1104/pp.33.6.385.

Merlin, M., Solarik, K.A., Landhäusser, S.M., 2020. Quantification of uncertainties introduced by data-processing procedures of sap flow measurements using the cut-tree method on a large mature tree. Agric. For. Meteorol. 287, 107926. https://doi.org/10.1016/j.agrformet.2020.107926.

Newbery, D.M., Schwan, S., Chuyong, G.B., van der Burgt, X.M., 2009. Buttress form of the central African rain forest tree *Microberlinia bisulcata*, and its possible role in nutrient acquisition. Trees 23 (2), 219–234. https://doi.org/10.1007/s00468-008-0270-3.

Ngomanda, A., Mavouroulou, Q.M., Obiang, N.L.E., Iponga, D.M., Mavoungou, J.-F., Lépengué, N., Picard, N., Mbatchi, B., 2012. Derivation of diameter measurements for buttressed trees, an example from Gabon. J. Trop. Ecol. 28 (3), 299–302. https://doi.org/10.1017/S0266467412000144.

Nogueira, E.M., Nelson, B.W., Fearnside, P.M., 2006. Volume and biomass of trees in central Amazonia: influence of irregularly shaped and hollow trunks. For. Ecol. Manage 227 (1), 14–21. https://doi.org/10.1016/j.foreco.2006.02.004.
Pebesma, E., Bivand, R., 2023. Spatial Data Science: With Applications in R, 1st ed. Chapman and Hall/CRC, New York, p. 314. https://doi.org/10.1201/9780429459016.
Pebesma, E., 2018. Simple features for R: standardized support for spatial vector data. R. J. 10 (1), 439. https://doi.org/10.32614/RJ-2018-009.
Pebesma, E., 2025. lwgeom: Bindings to Selected "liblwgeom" Functions for Simple Features (Version 0.2-15) [R]. https://r-spatial.github.io/lwgeom/.
R Core Team, 2025. R: A Language and Environment for Statistical Computing (Version 4.5.0) [Computer Software]. R Foundation for Statistical Computing, Vienna. www.R-project.org.
Rock, J.F., 1916. Palmyra Island with a Description of Its Flora. College of Hawaii Publications, Honolulu, HI, p. 53.
Roupsard, O., Bonnefond, J.-M., Irvine, M., Berbigier, P., Nouvellon, Y., Dauzat, J., Taga, S., Hamel, O., Jourdan, C., Saint-André, L., Mialet-Serra, I., Labouisse, J.-P., Epron, D., Joffre, R., Braconnier, S., Rouzière, A., Navarro, M., Bouillet, J.-P., 2006. Partitioning energy and evapo-transpiration above and below a tropical palm canopy. Agric. For. Meteorol. 139 (3), 252–268. https://doi.org/10.1016/j.agrformet.2006.07.006.
Shinohara, Y., Tsuruta, K., Ogura, A., Noto, F., Komatsu, H., Otsuki, K., Maruyama, T., 2013. Azimuthal and radial variations in sap flux density and effects on stand-scale transpiration estimates in a Japanese cedar forest. Tree Physiol. 33 (5), 550–558. https://doi.org/10.1093/treephys/tpt029.
Smith, A.P., 1972. Butteressing of tropical trees: a descriptive model and new hypotheses. Am. Nat. 106 (947), 32–46. https://doi.org/10.1086/282749.
Steppe, K., De Pauw, D.J.W., Doody, T.M., Teskey, R.O., 2010. A comparison of sap flux density using thermal dissipation, heat pulse velocity and heat field deformation methods. Agric. For. Meteorol. 150 (7), 1046–1056. https://doi.org/10.1016/j.agrformet.2010.04.004.
Vandegehuchte, M., Steppe, K., 2012. Improving sap flux density measurements by correctly determining thermal diffusivity, differentiating between bound and unbound water. Tree Physiol. 32, 930–942. https://doi.org/10.1093/treephys/tps034.
Walker, T.A., 1991. Pisonia islands of the Great Barrier Reef. Part I. The distribution, abundance and dispersal by seabirds of *Pisonia grandis*. Atoll. Res. Bull. 350, 1–23.
Wiens, H.J., 1962. Atoll Environment and Ecology. Yale University Press, New Haven, CT, p. 532.
Zunic, J., Rosin, P.L., 2004. A new convexity measure for polygons. IEEE Trans. Pattern. Anal. Mach. Intell. 26 (7), 923–934. https://doi.org/10.1109/TPAMI.2004.19.